Contents lists available at ScienceDirect

Additive Manufacturing

journal homepage: www.elsevier.com/locate/addma

Research paper

Large-scale additive manufacturing of optimally-embedded spinodal material architectures

Andrea Nale [a] , Andrea Chiozzi [b],*, Fernando V. Senhora [c] , Glaucio H. Paulino [d,e,*]

[a] Department of Architecture, University of Ferrara, Via della Ghiara 36, Ferrara, 44121, Italy
[b] Department of Environmental and Prevention Sciences, University of Ferrara, C.so Ercole I d'Este 32, Ferrara, 44121, Italy
[c] School of Civil and Environmental Engineering, Georgia Institute of Technology, 790 Atlantic Drive NW, Atlanta, 30332, GA, USA
[d] Department of Civil and Environmental Engineering, Princeton University, Engineering Quadrangle, Princeton, 08540, NJ, USA
[e] Princeton Materials Institute (PMI), 70 Prospect Ave, Princeton, 08540, NJ, USA

ARTICLE INFO

ABSTRACT

We present a synergistic methodology to design large-scale 3D-printed structures based on a multi-material topology optimization formulation, which leads to the realization of three-dimensional hierarchical structures with spatially oriented non-periodic spinodal microstructures. The inherent characteristics of these unstructured architectures allow the design of optimized layouts with smooth transitions of spinodal material classes, accounting for varying porosity and orientation. The design and manufacturing processes are bridged by a topology-by-material optimization approach, in which the iterative process preserves the macro-scale continuity, while the microstructural topological space is optimized by a suitable distribution of multiple spinodal architected materials. To illustrate both the design and the manufacturing processes, we leverage the features of a large-scale water jetting powder-bed 3D printing technology, which makes use of aggregates obtained from powdered stone-like materials and magnesium-based binders. The optimized model is transferred to the printer by means of a voxel-based generation strategy. The approach, exemplified by means of several numerical simulations and physical 3D-printed samples, connects design conceptualization, material properties at different length scales, and the complex process of additively manufacturing load-bearing structures in a large-scale framework.

1. Introduction

The process of designing structures involves a complex interaction between architecture and engineering. In this context, noteworthy structural elements, which play a singular role in civil engineering, are arches, vaults, domes, and general shells [1]. Such structures are usually inherently self-supported [2] and historically served not only structural purposes but also social, cultural, and religious functions. Example of self-supported structures can be traced back to ancient times. An exemplary instance is The Pantheon, built between 75–138 AD, showcasing the Roman innovation to find design solutions to build large-structures with materials exhibiting negligible tensile strength. Indeed, the temple was made by pozzolanic concrete and is faced with stones or bricks [3]. Another remarkable example is the Hagia Sophia's basilica, built during the Byzantine period in Constantinople.

The design of self supporting arches was later rigorously investigated by the English engineer Robert Hooke during the 16th Century. The principle behind his substantial contribution is summarized by the statement *"As hangs the flexible line, so but inverted will stand the rigid arch"*, later known as Hooke's second law. A more recent and most notable example of ingenious use of self supporting structures is found in Antonio Gaudí's architectural creations, which frequently resorted to the use of the catenary arch [4]. Drawing inspiration from Hooke's work, Gaudí designed the well-known civil building of Casa Milà and Sagrada Familia in Barcelona, Spain.

Inspired by these historical structures, in the present work, a multi-scale topology optimization methodology is proposed for the design of innovative large-scale self-supported 3D structures, which can be produced by additive manufacturing using no-tension stone-like materials by means of an innovative water jetting powder-bed 3D printing technology. Large-scale additive manufacturing has recently opened up new horizons for the construction sector [5]. Not only have these developments revolutionized the manufacturing process of structures, but also allowed the introduction of novel ways of enhancing sustainability in the construction sector [6,7]. The cement industry is

---

* Corresponding authors.
E-mail addresses: andrea.nale@unife.it (A. Nale), andrea.chiozzi@unife.it (A. Chiozzi), fsenhora3@gatech.edu (F.V. Senhora), gpaulino@princeton.edu (G.H. Paulino).

known for being one the most energy-intensive activities [8], hence prompting the exploration of alternative materials, such as those made from recycled raw materials and waste [9]. However, there is a pressing need for computational tools capable of systematically harnessing the design freedom offered by additive manufacturing. Addressing such need, topology optimization has emerged as a branch of structural optimization capable of providing rational solutions for design processes [10], encompassing various numerical strategies aimed at maximizing stiffness, minimizing weight, or addressing multiphysics problems, including acoustic or thermal coupled problems. However, topology optimization of large-scale structures remains a challenging endeavor.

The development of additive manufacturing technologies enables printing at different length scales and, due to its capabilities of reproducing complex microstructures, has fostered the design of materials with improved mechanical, thermal and electrical performances, while prompting a revival of multi-scale topology optimization approaches [11,12]. The varieties of small-scale biological and natural systems, *e.g.* termite nets [13], honeycomb [14], venus flower basket [15], have inspired the conception of several architected materials. A common and straightforward design for microstructures is based on periodic patterns, such as strut-based [16] or plate-based [17] arrangements, which also shows similarities with the concept of functionally graded materials (FGMs) [18]. The potential applications of architected materials generated a growing interest towards manufacturing innovative components for sectors where high-performances are required, such as the biomedical [19] and aerospace [20] sector. The use of architected materials based on periodic microstructures requires the development of suitable strategies that allow continuity in the structure. For instance, in the case of strut-based microstructures, the introduction of connectivity indexes [21], convolution filters [22] or transition planes [23], has been proposed to avoid load distributions issues stemming from high stress concentrations at the connections. An alternative to standard lattice-based microstructures is provided by surface-based microstructures, such as triply periodic minimal surfaces (TPMS) [16]. Indeed, these architectures safeguard structural continuity through an interpolation function, circumventing the need for complex connectivity strategies. In particular, stress concentrations are avoided by adopting double curved surfaces and the smooth continuity between cellular materials. Despite these advantages, such microstructures are still periodic, which are particularly susceptible to fabrication limits and do not provide significant design freedom in terms of stiffness properties. Hence, several works have been redirecting the attention towards non-periodic systems. An example is the strut-based non-periodic material developed in [24] starting from unit periodic microstructures or the use of TPMS [25] that allows the design of functionally graded non-periodic cellular materials.

Recently, non-periodic architectures with anisotropic and isotropic behavior have been proposed by exploiting an analogy with the thermodynamic phenomena of spinodal decomposition [26]. Such materials, coined as spinodal architected materials, show structural and functional features [27,28] that allow easy programming of a given anisotropic behavior and, consequently, a straightforward classification of spinodal microstructures based on their macroscopic elastic features, *e.g.* lamellar, columnar, cubic. Spinodal microstructures are defined by a phase field in the form of a gaussian random field, hence allowing improved connectivity and smooth transitions between different material classes [29]. Consequently, the provided structural continuity combined with a non-periodic microstructural pattern allows to generate structures more resilient to fabrication imperfections [30].

Another crucial aspect regards the manufacturing of large-scale objects [31], which recently received attention on employing cement-based materials [5]. The applications of these technologies mainly targeted the construction sector allowing the manufacturing of both structural and non-structural components [7]. Additive manufacturing techniques can be mainly subdivided in two main branches: deposition

and powder-bed methods. Deposition methods typically involve either extrusion or spraying techniques.

The extrusion method, widely used in additive manufacturing, deposits plastically deformable filaments layer-by-layer along a predetermined printing path. Key factors include material stiffness, influencing post-extrusion deformations, and filament dimensions such as cross-sectional area and aspect ratio. In contrast, spray-based concrete additive manufacturing utilizes a stream of compressed air to enable a layer-by-layer application of atomized material. An alternative approach to additively manufacture free-form large-scale structures is based on powder bed technology, which enables free-form large-scale structures through three strategies: binder jetting (BJ), selective paste intrusion (SPI), and selective cement activation (SCA). These technologies differ in the way the activator (A), the binder (B) and the aggregate (AG) are combined during the manufacturing process, as depicted in Fig. 1.

In this paper, we demonstrates the scalability of spinodal architectures in a large-scale additive manufacturing framework and its application to the conception of optimally designed self-supporting structures for civil engineering. In order to overcome the difficulties associated with large-scale structural optimization, we propose a multi-scale and multi-material compliance based topology optimization approach, which we denote by the expression *topology-by-material*, where the iterative process aims at optimizing the inner material distribution using multiple different spinodal architectures, allowing for varying porosity and orientation, while keeping the macro-scale domain topology fixed. Here, we tailor the approach on the features of an innovative water jetting powder-bed additive manufacturing technology that utilizes powdered stone-like waste materials from the construction industry, which exhibit negligible tension strength, as aggregates [37]. The limits imposed by the manufacturing technology are included as constraints in the optimization procedure. By targeting self-supporting structures, *e.g.* arches and vaults, we ensure that, at the macroscopic level, compression stress states prevail throughout the structure.

The paper is organized as follows: in Section 2, we provide an overview of the implemented non-periodic spinodal microstructures, followed by a comprehensive discussion of the proposed topology optimization approach, covering aspects such as formulation, problem setting, and the bridging of the computational optimization methodology presented to large-scale additive manufacturing; in Section 3, we illustrate and discuss the proposed topology optimization approach by means of meaningful numerical simulations, along with actual 3D prints of suitable spinodal samples; we close with a discussion of the outcomes of the proposed research and outline future developments in Sections 4 and 5.

2. Materials and methods

In order to design hierarchical 3D printed structures in a large-scale framework, we devise a multi-scale homogenization-based topology optimization strategy derived from [38] which couples design optimization techniques and manufacturing process to ensure the fabrication of the final layout. With the use of tailored spinodal microstructures, we are able to embed different materials with locally-varying anisotropic properties [30] into the optimized design, which is then manufactured by a voxel-based strategy. The remainder of this section presents the details of the methods and materials utilized in this work.

2.1. Non-periodic microstructures for large-scale additive manufacturing: spinodal architected materials

The phase field defining spinodal microstructural architectures used in the proposed topology optimization approach is computed by introducing a suitable gaussian random field (GRF) ψ. The functional approximation of the spinodal decomposition allows to set the anistropic
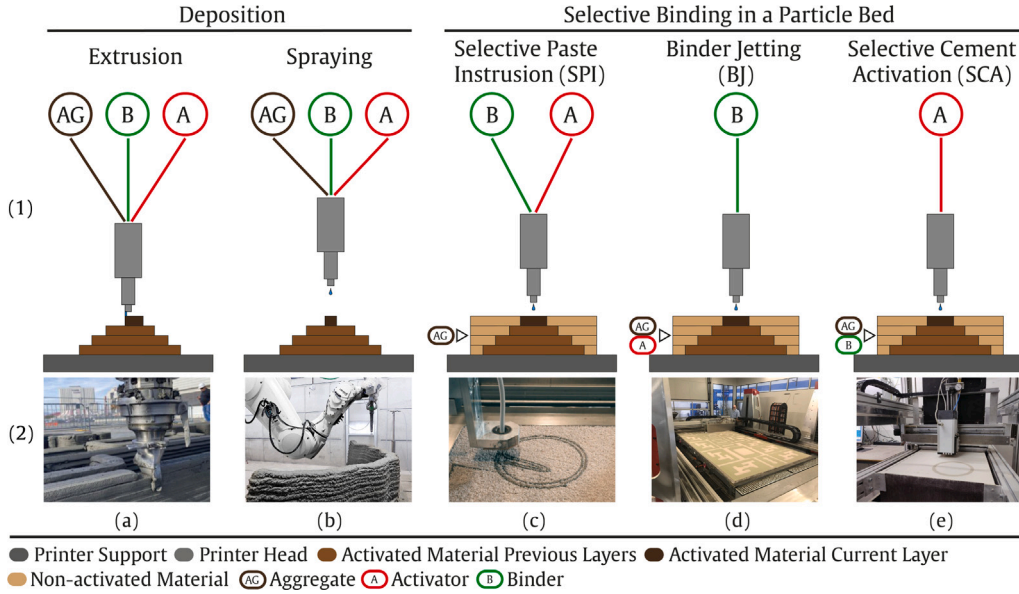
Fig. 1. Additive manufacturing technologies for 3D concrete printing. (1) Schematic overview of deposition and selective binding in powder bed technology for the fabrication of concrete formworks. (2) Examples of concrete 3D printing techniques: (a) extrusion by means of a rectangular nozzle with a gantry printer including side trowels [32], (b) spraying by a small nozzle of the cement paste accelerated by the addition of compressed air [33], (c) activation of an inert material by the intrusion of binder-activator paste (SPI) [34], (d) activation of a powder bed made by aggregate and activator by binder jetting (BJ) [35] and (e) layer by layer activation of an aggregate-binder mixture by means of the selective application of an activator (SCA) [36].

properties by manipulating the stochastic distribution of a set of vectors, *i.e.* the wave vectors $\mathbf{n}_i, i = 1, \ldots, N^w$, on a unit sphere $\mathbf{n}_i \in \mathcal{U}[\mathbb{S}^2]$. The wave vectors are defined as

$$\mathbf{n}_i \in \mathcal{U}[\{\mathbf{m} \in \mathbb{S}^2 : (|\mathbf{m} \cdot \hat{\mathbf{e}}_1| > \cos\theta_1) \oplus (|\mathbf{m} \cdot \hat{\mathbf{e}}_2| > \cos\theta_2) \oplus (|\mathbf{m} \cdot \hat{\mathbf{e}}_3| > \cos\theta_3)\}], \tag{1}$$

whose space is restricted by the angles $\theta_1, \theta_2, \theta_3 \in [0, \pi/2]$ on the unit sphere [39]. The wave vectors allow the computation of the GRF for each element $\ell = 1, \ldots, N^e$ as follows:

$$\psi(x_\ell) = \sqrt{\frac{2}{N^w}} \sum_{i=1}^{N^w} \cos(\zeta\mathbf{n}_i \cdot x_\ell + \omega_i), \tag{2}$$

in the Cartesian space $\mathbb{R}^3$ with basis $\{\hat{\mathbf{e}}_1, \hat{\mathbf{e}}_2, \hat{\mathbf{e}}_3\}$, where Eq. (2) represents a convenient definition of the spinodal phase decomposition [26]. Indeed, the manipulation of the GRF allows the definition of different anisotropic classes, each one with unique features. In addition, each anisotropic material is controlled by the amplitude, N^w, wavelength, ζ, and phase shift $\omega_i \in \mathcal{U}[0, 2\pi)$ of the ith wave, which is randomly sampled. Not only are materials based on spinodal architectures relevant for their mathematical construction, but also for their mechanical features [30], exhibiting different anisotropic behaviors for each class, as shown in Table 1, making them suitable for the design of structures with improved properties.

These microstructures are defined by a binary function ψ_ℓ, which defines solid and void regions,

$$\psi_\ell(x_\ell) = \begin{cases} 1 \text{ if } \psi_\ell(x_\ell) \geq \psi_{cut}(\rho_\ell) \\ 0 \text{ otherwise,} \end{cases} \tag{3}$$

and the density ρ_ℓ, which appears in the level-set function ψ_{cut}:

$$\psi_{cut}(\rho_\ell) = \sqrt{2}erf^{-1}(2\rho_\ell - 1). \tag{4}$$

The definition of the phase field in Eq. (2) requires the definition of a large number N^w of wave vectors $\mathbf{n}_i$, which mathematically represents the amplitude, being the field ψ statistically homogeneous when N^w tends to infinite. The phase shift of the generic wave i, $\omega_i \in \mathcal{U}[0, 2\pi)$, is sampled from a uniform distribution randomly.

The parameter ζ allows to set the length scale of spinodal features, thus defining the characteristic dimension of solid and void phases in the architecture at a given fixed density value. Finally, non-periodic materials can be oriented by adjusting the wave vectors $\mathbf{n}_i$ by means of the rotational angles $(\alpha_\ell, \beta_\ell, \gamma_\ell)$, which define the orientations of the reference frame satisfying the GRF restriction prescribed by angles $(\theta_1, \theta_2, \theta_3)$ in a three dimensional Cartesian space.
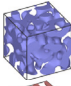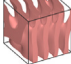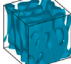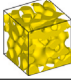
2.2. Topology-by-material: a new multi-material topology optimization formulation

The conventional topology optimization formulation involves minimization of compliance under volume constraints [10]. Within this framework, the optimal layout can attain any geometry within the defined domain and imposed boundary conditions. Moreover, during the optimization process, a variation of the topology occur so that the final layout is usually not topologically equivalent to the input domain anymore. Indeed, the optimization constraints, such as volume constraints, drive the iterative process to include holes, voids and cavities in the structure, which lead to regions in tension and compression and generally to truss-like solutions [40]. An extension and generalization of the classical approach can be found in multi-material topology optimization formulations [41], where the optimization process can simultaneously accommodate different materials to achieve an optimized layout composed by regions with different material properties.

Here, a multi-material multi-scale topology optimization approach is introduced to intertwine the microstructural features of the material, the design of the optimized structure and the manufacturing process. In this formulation, which we refer to as *topology-by-material*, illustrated in Fig. 2, the topology of the domain is safeguarded, while the iterative optimization process searches for optimal material placement, allowing for the coexistence at the micro-scale of a selected number of spinodal material classes in the optimal layout. The initial topology of the domain is preserved by setting an high volume fraction, $\bar{v}$, whereas the geometric space, where the optimal layout is sought, is set by assigning the initial geometry and may undergo changes during iterations in response to the applied volume constraint. In the proposed framework, classical homogenization theory [42] is employed to connect micro-

Table 1

Examples of spinodal architected materials for each implemented class by setting the following parameters: spinodal density, ρ, GRF angles restriction, $(\theta_1, \theta_2, \theta_3)$, orientation of reference frame, (α, β, γ), and wavelength, ζ.

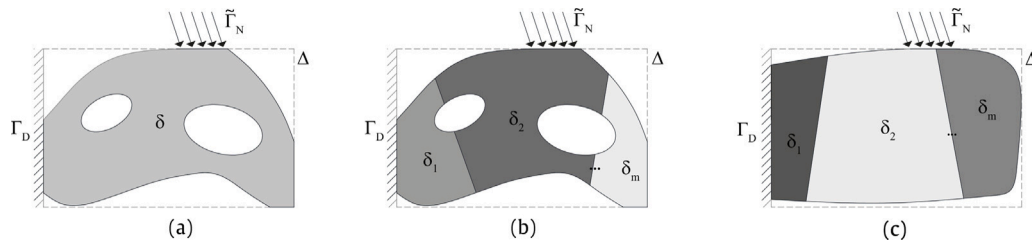| ρ []	Spinodal class	$\theta_1, \theta_2, \theta_3$ [°]	α, β, γ [°]	ζ [cm^{-1}]	Microstructure
0.4	*Isotropic*	(90,0,0)	(0,0,0)	4	
0.4	*Lamellar*	(0,30,0)	(0,0,0)	4	
0.4	*Columnar*	(30,30,0)	(0,0,0)	4	
0.4	*Cubic*	(30,30,30)	(0,0,0)	4	

Fig. 2. Illustration of material distribution with different optimization approaches with extended design domain and boundary conditions. (a) Single-material topology optimization, (b) multi-material topology optimization and (c) *topology-by-material* optimization.

and macro-scale, thereby providing the mechanical characteristics of various spinodal microstructures through their respective homogenized material elasticity tensor. The result of the optimization is a functionally graded structure featuring a seamless transition between different spinodal material classes, with varying porosity and density features. Such methodology holds potential in the exploration of new optimized layouts and solutions for self-supported structures, bridging civil engineering with innovative large-scale additive manufacturing processes for concrete-like materials.

The optimal layout, δ, includes the union of a finite number of distinct, non-intersecting sets, $\delta = \cup_i^m \delta_i$, $\delta_i \cap \delta_j = \emptyset$ for $i \neq j$. The number of these partitions δ_i is at most equal to the number of candidate materials, N^m, in the extended domain $\Delta \subseteq \mathcal{R}^2$. In the extended domain, as shown in Fig. 2, Γ_D and $\tilde{\Gamma}_N \subseteq \Gamma_N$ represents respectively the partition of $\partial\Omega$ on which displacements and non-zero tractions are prescribed.

The topology-by-material optimization approach, see the nomenclature in Appendix C, enables to accommodate many local or global volume constraints [43], minimizing the compliance by constraining the volume. The problem is stated as follows:

$$\min_{\mathbf{Z},\rho,\alpha,\beta,\gamma} \quad f = \mathbf{F}^T \mathbf{U}(\mathbf{Z},\rho,\alpha,\beta,\gamma),$$

$$\text{s.t.} \quad g_j = \frac{\sum_{m \in \mathcal{G}_j} \sum_{\ell \in \mathcal{E}_j} V_\ell m_v(y_{\ell m})}{\sum_{\ell \in \mathcal{E}_j} V_\ell} - \overline{v}_j \leq 0, \quad j = 1, \dots, N^c, \quad (5)$$

$$\text{with} \quad \mathbf{K}(\mathbf{Z},\rho,\alpha,\beta,\gamma)\,\mathbf{U}(\mathbf{Z},\rho,\alpha,\beta,\gamma) = \mathbf{F},$$

where $\overline{v}_j = \sum_{i \in \mathcal{G}_j} \sum_{\ell \in \mathcal{E}_j} V_\ell m_v(y_{\ell m}) / \sum_{\ell \in \mathcal{E}_j} V_\ell$ allows to restrict the design space reducing the total volume of the assigned domain, optimally distributing and orienting the material. The design variables field is composed by the material composition, $\mathbf{Z} = \{z_{\ell 1}, \dots, z_{\ell N^m}\}_{\ell=1}^{N^e}$, which is defined for each material, $m = 1, \dots, N^m$, and the microscopic spinodal features, $(\rho, \alpha, \beta, \gamma)$, which is defined by the spinodal density $\rho = \{\rho_1, \dots, \rho_{N^e}\}$ and the orientations of the selected candidate material $\alpha = \{\alpha_{\ell 1}, \dots, \alpha_{\ell N^m}\}_{\ell=1}^{N^e}$, $\beta = \{\beta_{\ell 1}, \dots, \beta_{\ell N^m}\}_{\ell=1}^{N^e}$, $\gamma = \{\gamma_{\ell 1}, \dots, \gamma_{\ell N^m}\}_{\ell=1}^{N^e}$. Here, the definition of rotational angles of the reference frame for each element and candidate material allows to properly orient the microstructures. Indeed, a unique design variable angle could move the

optimization to a different local minimum due to multiple coexisting materials, which typically happens at the interfaces. In this case, a single angle may not be sufficient to optimally orient multiple materials. By the introduction of more design angle variables, it is possible to well-orient each candidate material and select the best fit for each element avoiding multiple materials in the same element.

The elemental density field, $\mathbf{Y} = \{y_{1m}, \dots, y_{\ell m}\}_{m=1}^{N^m}$, is regularized by a filter [44,45] of order q and radius R, which enforces a well-posed problem by a regularization map between the centroids of elements i and j:

$$P_{ij} = \frac{max[0,(R - \|\mathbf{x}_i - \mathbf{x}_j\|_2)^q]V_j}{\sum_{k=1}^{N^e} max[0,(R - \|\mathbf{x}_i - \mathbf{x}_k\|_2)^q]V_k}, \quad (6)$$

which is coupled with a Heaviside projection $\tilde{\mathbf{Y}} = \{\tilde{y}_{1m}, \dots \tilde{y}_{\ell m}\}_{m=1}^{N^m}$ [46]. The filtering technique is combined with a penalization scheme based on a continuation approach. The penalization factor is increased after each penalization step, when the convergence or the maximum number of iterations are reached. The structural compliance problem is started by setting the penalization factor and the material mixing, respectively $p = 1$ and $\tau = 0$. The choice is motivated by previous work [43], which demonstrated the effectiveness of a continuation scheme with multi-material optimization. Although the optimization problem Eq. (5) is no longer convex due to presence of angle orientation, the continuation scheme showed eases the convergence to local minimum by gradually reducing the amount of intermediate density. Then, the penalization factor is increased at each penalization step to reach a better optimal layout. The continuation scheme leads to a local minimum with a better approximation of the material distribution. Thus, the filtered density field, $\tilde{\mathbf{Y}}$, is penalized through a SIMP interpolation scheme [41] to enforce the penalization of intermediate values $\mathbf{W} = \{w_{1m}, \dots, w_{\ell m}\}_{m=1}^{N^m}$, where $w_{\ell m} = \tilde{y}_{\ell m}^p$.

The formulation, defined in Eq. (5), allows us to include local constraints by means of two groups of indices $\mathcal{G}_j$ and $\mathcal{E}_j$, which respectively control the materials and elements associated to constraints $j = 1, \dots, N^c$. Furthermore, we indicate by $v_{\ell m} = y_{\ell m}\rho_\ell$ the volume of element ℓ associated to material m, which depends on the density of each candidate material ρ_ℓ and the filtered material composition

field. The optimization problem is solved with the same finite element discretization adopted to solve the state equations of static elasticity $\mathbf{K}(\mathbf{Z}, \rho, \boldsymbol{\alpha}, \boldsymbol{\beta}, \boldsymbol{\gamma}) \mathbf{U}(\mathbf{Z}, \rho, \boldsymbol{\alpha}, \boldsymbol{\beta}, \boldsymbol{\gamma}) = \mathbf{F}$, where $\mathbf{U}$ is the displacement field, $\mathbf{F}$ is the design-independent nodal loads vector and $\mathbf{K}$ is the global stiffness matrix assembled from the local element stiffness matrices $\mathbf{K}_\ell(Z_{\ell m}, \rho_{\ell m}, \alpha_{\ell m}, \beta_{\ell m}, \gamma_{\ell m})$. The objective function, f, is computed by solving the finite element state equation in linear elasticity:

$$\mathbf{K}(\mathbf{Z}, \rho, \boldsymbol{\alpha}, \boldsymbol{\beta}, \boldsymbol{\gamma})\mathbf{U} = \mathbf{F} \tag{7}$$

The local elemental stiffness matrix for linear basis functions [47] is defined as:

$$\mathbf{K}_\ell = \int_{\Omega_\ell} \mathbf{B}^T \mathbf{D}_\ell(\mathbf{Z}_\ell, \rho_\ell, \alpha_\ell, \beta_\ell, \gamma_\ell) \mathbf{B} d\mathbf{x}, \tag{8}$$

where $\mathbf{B}$ is the element-strain displacement matrix, while $\mathbf{D}_\ell$ is the elastic material matrix obtained by multi-material interpolation of m homogenized candidate materials in the reference frame for each element ℓ. The material properties of element ℓ are interpolated by the following multi-material interpolation function:

$$\mathbf{D}_\ell = \sum_{m=1}^{N^m} w_{\ell m} \prod_{\substack{q=1 \\ q \neq m}}^{N^m} (1 - \tau w_{\ell q}) \mathbf{M}(\alpha_{\ell m}, \beta_{\ell m}, \gamma_{\ell m}) \mathbf{D}_m^H(\rho_{\ell m}) \mathbf{M}^T(\alpha_{\ell m}, \beta_{\ell m}, \gamma_{\ell m}). \tag{9}$$

where $p > 1$ (SIMP) [41] and $0 < \tau < 1$ represents, respectively, the single-material and the material mixing penalization factors. The first is introduced to penalize intermediate densities, $\mathbf{W}$, while the second to control the allowable mixing [43,48]. The parameters are gradually increased during the iteration steps to prevent intermediate single material densities and small mixing regions, which may occur at material interfaces as undesired artifacts of the density filter used in topology optimization. Such artifacts may hinder convergence and are penalized, in order to avoid intermediate or non-physical material states (*i.e.*, densities greater than one at any given point) and numerical instabilities.

The homogenized stiffness elasticity matrix, $\mathbf{D}_m^H$, in the reference frame (non-oriented) reads:

$$(\mathbf{D}_m^H)_{ij}(\rho_\ell) = (\mathcal{F}_m)_{ij}(\rho_\ell), \tag{10}$$

where $(\mathcal{F}_m)_{ij}(\rho_\ell)$ is the fourth order polynomial function detailed in Section 3.2. Then, the material matrix is oriented in the rotated frame via the tensor transformation laws for stress and strains, respectively $\{\sigma\}' = \mathbf{M}\{\sigma\}$ and $\{\epsilon\}' = \mathbf{M}^T\{\epsilon\}$, where the rotation matrix $\mathbf{M}(\alpha_{\ell m}, \beta_{\ell m}, \gamma_{\ell m})$ is defined in Appendix A.

2.3. Gradient-based solution scheme

The optimization problem stated in Eq. (5) is solved by a gradient-based solution scheme. To solve the structural compliance problem the evaluation of sensitivities for objective function and constraints are computed as illustrated in Appendix B. The derivatives guide the iterative process into an optimal local minimum design. Here, the augmented lagrangian (AL) method [49], a numerical technique for solving constrained optimization problems, is adopted. The augmented lagrangian function reads:

$$\mathcal{L}(\mathbf{x})^{(\mathbf{t})} = f(\mathbf{x}) + \sum_{j=1}^{K} [\lambda_j^{(t)} \max(g_j(x), -\frac{\lambda_j^{(t)}}{\mu^{(t)}}) + \frac{\mu^{(t)}}{2} max(g_j(x), -\frac{\lambda_j^{(t)}}{\mu^{(t)}})^2], \tag{11}$$

which is minimized in each outer iteration t as the sum of objective function, *i.e.* the compliance, and a penalty term containing the original constraints $g_j, j = 1, \dots, K$. The penalization parameters, $\lambda_j^{(t)}$ and $\mu^{(t)}$,

are updated every 5 interactions as:

$$\lambda_j^{(t+1)} = \lambda_j^{(t)} + \mu^{(t)} \max(g_j^{(t)}(\mathbf{x}), -\frac{\lambda_j^{(t)}}{\mu^{(t)}}) \ and \ \mu^{(t+1)} = 1.25\mu^{(t)}. \tag{12}$$

The design variables $\mathbf{x}$ are updated at each inner optimization iteration, k. The AL method is combined with the Steepest Descent Method (SDM) [50], a mathematical programming technique able to handle bound constraints by the following update rule:

$$\mathbf{x}^{(k+1)} = \max[\min(\mathbf{x}^{(k)} - t^{(k)}\frac{\partial \mathcal{L}^{(k)}}{\partial \mathbf{x}}, \mathbf{x}^{(k)} + mv_{(*)}), \mathbf{x}^{(k)} - mv_{(*)}], \tag{13}$$

where $mv_{(*)}$ is move limit, where $_{(*)}$ assumes notation Z for material design variable and $\{\alpha, \beta, \gamma\}$ for orientation design variable, and $t^{(k+1)} = \max(0.99t^{(k)}, 0.01)$ is the step size with $t^{(0)} = 1$.

2.4. Bridging topology-by-material optimization with large-scale additive manufacturing

The output of a multi-scale and multi-material optimization problem needs to be post-processed. Here, a post-processing procedure is used to efficiently link the visualization and the manufacturing of complex structures. One of the main challenges of designing hierarchical structures is the connectivity. Smooth continuity is achieved by a voxel-based strategy, which entails the subdivision of the optimized layout into homogeneous material regions $\mathcal{B}_i$. The design variables in the 3D discretized space, *i.e.* the filtered composition material $\mathbf{Y}$, the density ρ and the orientations $\boldsymbol{\alpha}, \boldsymbol{\beta}, \boldsymbol{\gamma}$ are projected into a finer mesh, called voxel-grid. The projected fields $\tilde{\mathbf{z}}, \tilde{\rho}, \tilde{\alpha}, \tilde{\beta}$ and $\tilde{\gamma}$ are embedded by a discrete form of the GRF:

$$\psi_{lm}^0(\mathbf{x}_\ell) = \sqrt{\frac{2}{N^w}} \sum_{k=1}^{N^w} \cos(\zeta[\mathbf{R}(\tilde{\alpha}_{\ell m}, \tilde{\beta}_{\ell m}, \tilde{\gamma}_{\ell m})\mathbf{n}_{km}] \cdot \tilde{\mathbf{x}}_\ell + \omega_k), \tag{14}$$

where the precomputed wave vectors $\mathbf{n}_{ki}$ of the candidate spinodal microstructure m, according to the angular restrictions $(\theta_1, \theta_2, \theta_3)$ of the GRF, are properly rotated by the projected optimized angles values $(\tilde{\alpha}_{\ell m}, \tilde{\beta}_{\ell m}, \tilde{\gamma}_{\ell m})$ without any smoothing. Then, the homogeneous material fields are interpolated between each other to enforce a gradual and smooth connectivity as follows:

$$\psi_\ell(\tilde{\mathbf{x}}_\ell) = \frac{\sum_{m=1}^{N^m} \max[0, (1 - \frac{d_H(\tilde{x}_\ell, \mathcal{B}_m)}{R_\psi})]^{1/2} \psi_{\ell m}^0(\tilde{x}_{li}, \tilde{\alpha}_{\ell m}, \tilde{\beta}_{\ell m}, \tilde{\gamma}_{\ell m})}{\sum_{m=1}^{N^m} \max[0, (1 - \frac{d_H(\tilde{x}_\ell, \mathcal{B}_m)}{R_\psi})]^{0.5}}, \tag{15}$$

where d_H is the Hausdorff distance, R_ψ is the radius of the interpolated phase field and 0.5 is the penalization exponent. Finally, the obtained global phase field, ϕ_ℓ, defined in Eq. (15), is interpreted with solid and void phases via a level-set function:

$$\psi_\ell(\tilde{\mathbf{x}}_\ell) = \begin{cases} 1 \text{ if } \psi_\ell(\tilde{\mathbf{x}}_\ell) \geq \psi_{cut}(\tilde{\rho}_\ell) \\ 0 \text{ otherwise.} \end{cases} \tag{16}$$

The illustrated strategy allows to design large-scale spinodal architectures with smooth connectivity and efficiently link the outcome of the optimization process with additive manufacturing technology by adequately setting the post-processing parameters to the printer features.

2.5. Powder-bed large-scale additive manufacturing: materials and manufacturing process

The recent development of additive manufacturing technologies has also motivated the production of large-scale objects [31] using cement-based materials [5]. In this work, we focus on proposing a powder-bed technology to manufacture physical samples of non periodic 3D printed architected structures. Powder bed technology supports complex geometries with high resolution and mechanical stability due to the dry particle bed. It avoids gravitational flow issues typical of extrusion but demands significant material volume and space, raising economic and

environmental concerns. Innovations like magnesium-based cement and geopolymers aim to improve sustainability by enabling material reuse and reducing costs. Here, we adopt a selective cement activation on powder-bed technology to manufacture physical samples of non periodic 3D printed architected structures. The activator is a saline water-admixture solution, which selects the particle to activate on each thin layer according to a binary input file. The printing procedure, as illustrated briefly in Fig. 3, begins with the slicing of the 3D model into layers by an in-house software. The layers thickness is set according to a machine range of 5–10 mm. The slicer provides an instruction code, which is sent to the control panel and transmits the information to the printer head in order to control the opening and closing of the nozzles. Each layer is prepared by using a recoater and a sand feeder. Consequently, the material is distributed uniformly in the powder-bed in the x-y plane with a certain volume of the set thickness layer. The result is a flat surface leveled according to the selected layer thickness. Then, the printer head moves while selectively dropping droplets of water solution on the regions where the powder layer intersects the printed object. The remained non-activated powder acts as a support for the following layer and the activated voxels, where the chemical reaction is in progress.

The printing process is repeated until the total number of layers is completed. This procedure allows to print fully three-dimensional structures, where each layer behaves as a natural support for the next one. The design freedom enables the manufacturing of enclosed or cross-linked structures with some design limitations to allow the removal of the surplus of non-activated powder and guarantee the continuity of the printed object after removing the exceeding material. The printer is provided with a frame, which allow the printer head to reach a certain level from the ground, which is not perfectly flat. So, a flat surface to allow stability for the process and a good manufacturability to the object is required. Moreover, some supports are needed to withstand the large weight of the object during the manufacturing process and post-processing. Here, the printer used to fabricate the physical models is the Desa1 150.150, which is located in the headquarters of Desamanera S.r.l. (Rovigo, Italy). It has a Cartesian gantry system forming a box of 1.5 m³. The printing envelope has a square area of 1.5 m × 1.5 m with a square frame around the printing area. The frame is composed by four columns, each one equipped by an electric motor allowing the movement of the printer head along the vertical axis. Each column can be extended if necessary. The columns are fixed by beams on the bottom and on the top, which provide stability to the printer. Across the printable area there is a *middle* beam, which allows the movement of the printer head and the recoater, which is perpendicular to double beams. These are provided with another electric motor, which carries the printer head along each beam. The printable area results covered by a one direction movement by a single row of nozzles, which allow to run up and down the double beams. The deposition system is composed by 264 nozzles with an internal diameter of 5.7 mm, where each one controls a 5.7 mm thick line. The printer head is made by a serial of nozzles placed in a straight line. The nozzles are rowed across the whole printer and the swiping is allowed by electric motors located on the furthest point of the printer head.

The single voxel is activated by a saline solution, which is pressurized in a feeding tank. The liquid, which sits in a container nearby the printer has a pump to deliver steadily the liquid through a tube to the feeding tank under pressure. The liquid is sent to the printer head by a hose connected the tank. In the printer head, each nozzle has a valve controlled electronically to regulate the opening and the closing of the liquid. A sequence control the switching on and off during the movement. The dimensions of activated voxel are 5.7 mm × 5.7 mm in the Cartesian plane x-y and together with a layer height of 5.7 mm provide the printer resolution. The accuracy is related to the grain size distribution, the quantity and properties of the binder, while the printer head speed is linked to the deposit of dry mixture and the swipe motion

of nozzles. In addition, the time required to complete a layer is reduced by using a sand feeder, which is refilled manually, after each layer, by a pressurized tank connected to the feeder. Hence, the powder drops on the next layer and by using a recoater it is spread automatically. The motion of the printer head to drop the water solution is slower then the material distribution to avoid wrong positioning. The average speed of the printer is around 1 m³ / 0.5 h, *i.e.* approximately 2 min/layer. Once the last layer is completed, the object needs to be extracted. The structure during the printing process is supported by some formworks surrounding the boundaries of the powder-bed. These formworks prevented horizontal movements of the lower layers, which could be caused by the weight of the powder-bed. The complexity of the object and the quantity of non-activated material surrounding the object define the post-processing time. Post-processing entails object extraction, cleaning, air blowing, wetting and drying. Object extraction and cleaning is usually facilitated by the use of a powerful industrial vacuum cleaner. The object is cleaned by using tools to remove the unconsolidated material near the surface of the printed object, and all the exceeding material is reusable for a next printing. Then, air blowing allows to remove the last remained film of non-activated material. The printed object is finally washed with clean water and dried at environmental temperature.

The printed material is composed by the aggregate, *i.e.* the inert component, the binder, *i.e.* the cement, and the activator, *i.e.* the water-admixture solution. Differently from traditional 3D printed concrete, this approach avoids the creation of a workable paste, where all components are continuously mixed. Consequently, analyzing the printing process, it is possible to observe that the final result is a layered concrete, which has different characteristics than regular mixed concrete. These distinctions are related to the structure, where the layered concrete is built up layer-by-layer. It allows to maximize the material placement and to tailor internal geometries and optimized load-bearing capabilities. As a result, the deposition influences the material isotropy properties compared to conventionally mixed concrete. Hence, it is necessary to ensure a suitable and consistent inter-layer adhesion and material properties throughout the structure to preserve integrity. In addition, the layered concrete provides design flexibility, which is not only limited to the fabrication of complex geometries which are unachievable with traditional methods, but also on the optimal usage of material with respect to structural performances. Moreover, the powder bed water jetting technology allows the use of very different aggregates, *i.e.* marbles, stones, minerals and other stone-like materials from recycled waste from the construction industry, and binders, *i.e.* traditional Portland cement, magnesium or geopolymers. The flexibility provided in terms of materials also allows the manufacturing of sustainable structures by using eco-compatible binders. In addition, the use of magnesia cement, or magnesium oxychloride, allows to reach superior properties with respect to tradition Portland cement [52]. Other advantages have been demonstrated over regular magnesia concrete such as high fire resistance, thermo-insulating properties, good resistance to abrasion, etc. The powder formulation adopted in this contribution is prepared by mixing MgO (magnesium oxide), with particle size shown in Fig. 4, and KH_2PO_4 (mono potassium phosphate), for the magnesium-based binder.

The aggregate is a local river sand with fine particle size between 0.5–2 mm. The material consolidation after the chemical reaction of the magnesium oxide with mono potassium phosphate is the K-Struvite:

$$MgO + KH_2PO_4 + 5H_2O = MgKPO_4 \cdot 6H_2O, \qquad (17)$$
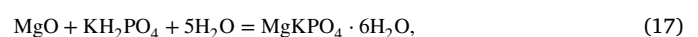
which represents the product of the MPC (magnesium potassium cement). The powder-bed mixture formulation [51] has mass fraction of 16.7 wt% for the binder MgO, 16.7 wt% for the MKP and 66.6 wt% for the sand aggregate. Water has molar ratio 3.38, which is consistent with regular magnesium potassium phosphate cement pastes [53].
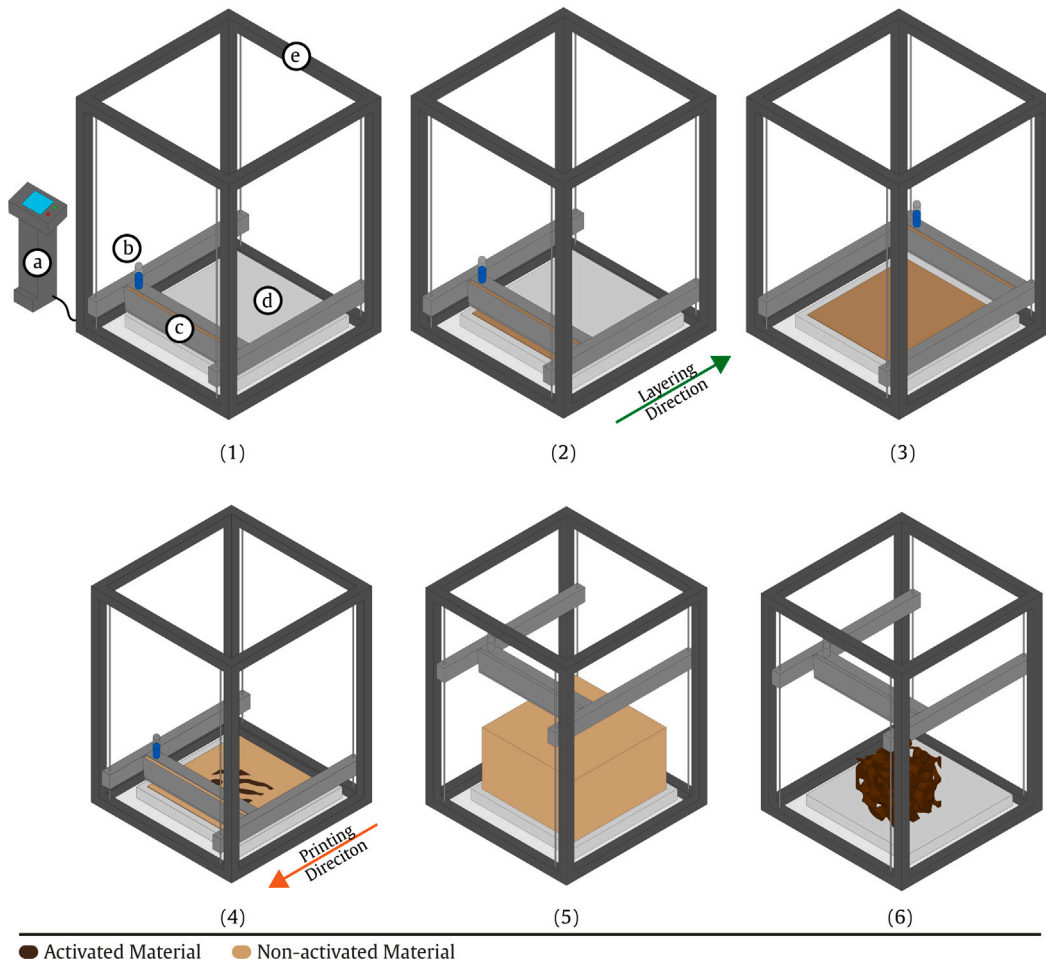
Fig. 3. Schematic 3D representation with trimetric view of the printing process. The printer process is summarized in the following steps as: (1) printer setup, (2) start material distribution for first layer, (3) end of material distribution for first layer, (4) activation of material for first layer, (5) the printing process continues until the n-layer and (6) the printing process ends and the object is extracted by a post-processing process. The printer components are detailed in the printer setup (1) where: (a) control panel, (b) water-jet printer head, (c) recoater, (d) printer envelope and (e) open-aluminum structures.
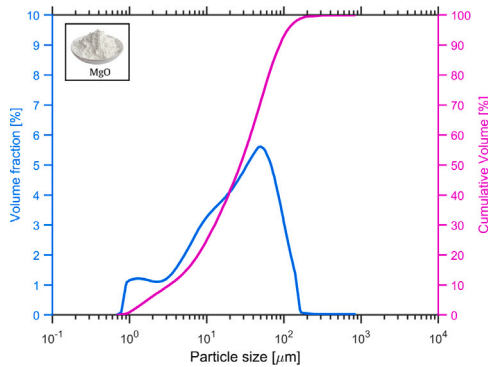

Fig. 4. Particle size distribution of the magnesium oxide (MgO), adapted from Gobbin et al. [51].

3. Results

Printing samples and numerical solutions are detailed in the following sub-sections. The manufacturing process is depicted by the upscale of Spinodal Architected Materials. So, physical models of Spinodal Architected Materials are presented using a water-jet powder-bed additive manufacturing technology. Finally, the *topology-material* optimization approach has been used to optimize self-supported structures with features compatible with the water jetting powder-bed additive manufacturing technique.

3.1. Scaling-up and manufacturing of spinodal architected materials

Powder-bed water jetting technique has been employed to manufacture spinodal architected materials with tunable anisotropy. These printing tests allow to identify specific features of the optimization process, *i.e.* the bounding manufacturing limit of density ρ, and the post-processing parameters, *i.e.* the length scale of voids through their wavelength ζ. As a result, such parameters are strictly related to the printer resolution and build volume of the object. Their estimation has been done by an iterative process by means of D-slicer, a suitable in-house software.

In particular, the spinodal density design variable must vary in a range from $\underline{\rho} = 0.4$ to $\bar{\rho} = 0.6$, in order to ensure manufacturability. Indeed, lower densities produce an high presence of voids, which is detrimental to the continuity of the spinodal architecture. On the other hand, for high densities, the voids are too small to allow high resolution of the cell structure. Moreover, manufacturability is related to the wavelength ζ of wavevectors, defined in Eq. (1), since the estimated wavelength ζ in the post-printing process is numerically close to the maximum dimension of the printed object. To evaluate the influence of such variable, large-scale printing tests of different spinodal architectures have been conducted. In particular, printed specimens have the dimension of a 300 mm × 300 mm × 300 mm cube. Such spinodal
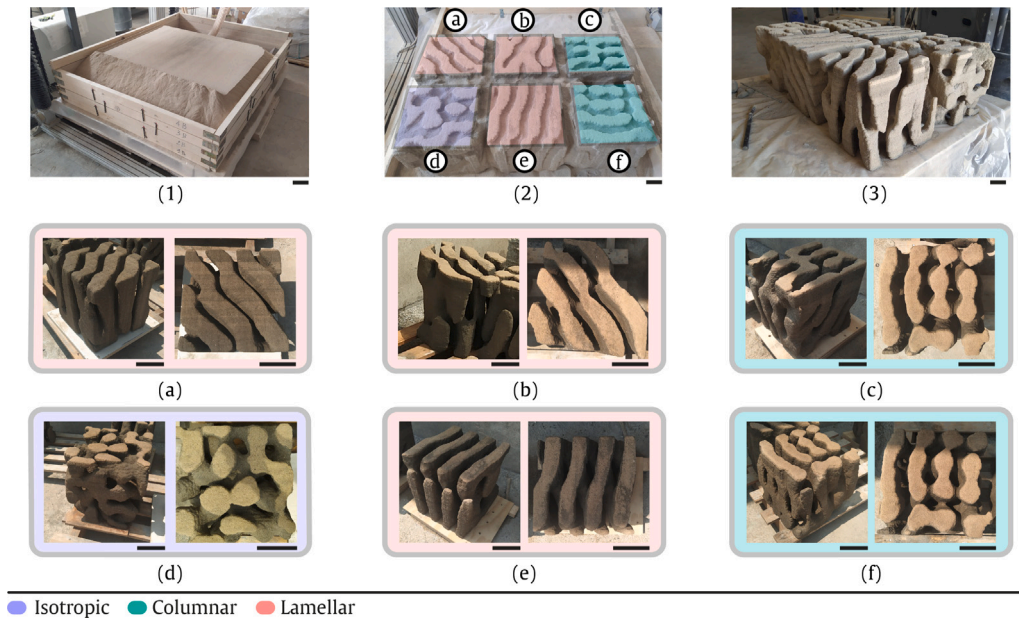
Fig. 5. Post-processing of spinodal cubes: (1) powder-bed; (2) extraction of cubes; (3) extracted cubes. The spinodal cubes are manufactured by a water-jetting powder-bed 3D printing technique varying the orientation of the reference frame, wavelength and density of the GRF: (a) lamellar material with 45° orientation with respect to the horizontal plane; (b) lamellar material with 45° orientation with respect to the vertical plane; (c) columnar material with 45° orientation with respect to the vertical plane; (d) isotropic material; (e) lamellar material with default orientation and (f) columnar material with 45° orientation with respect to the vertical plane. The scale bars at the bottom-right corner of each image represent 10 cm.

cubes, shown in Fig. 5, have been produced according to different wavelengths, $\zeta = 4$ cm^{-1} and $\zeta = 5$ cm^{-1}, in order to investigate the capability of the slicer to capture the microstructure. Moreover, a sample with a density higher than the manufacturability range has been produced to test the capability of the printer to properly activate the voxels representing the architecture of the material. In addition, some orientations have been chosen in order to investigate the ability to manufacture oriented non-periodic microstructures. In particular, the selected orientation along the y axis is defined by $\beta = 45°$ in the 3D cartesian space considering different classes of spinodal architectures, *i.e.* lamellar $(\theta_1, \theta_2, \theta_3) = (30°, 0°, 30°)$ and columnar $(\theta_1, \theta_2, \theta_3) = (0°, 30°, 0°)$.

3.2. Anisotropic homogenized properties

The multi-scale topology optimization formulation in Eq. (5) allows to handle any type of material by the homogenized material elasticity tensor, which has been computed using a MATLAB code [54]. The topology of different spinodal architected materials are defined by a level-set function, Eq. (3), on the GRF field, Eq. (2). Computational homogenization has been performed on an hexahedral element mesh of $10 \times 100 \times 100$ elements, adopting Young's modulus, E = 1, and Poisson's ratio, $\nu = 0.3$ for the bulk material.

The density variation of the spinodal microstructures in the optimization algorithm requires also to compute the material tensor of different spinodal densities. The homogenized stiffness elasticity matrix, $\mathbf{D}_m^H$, for material m in element ℓ is pre-computed for $\rho = 0.4, 0.5, 0.6$, where each component ij is fitted with a fourth-order polynomial of the form:

$$(\mathcal{F}_m)_{ij} = \sum_{s=0}^{4} (c_s)_{ij} \rho^s. \tag{18}$$

The coefficients c_s, where $s = 0, \ldots, 4$, allows to plot the fitted curves shown in Fig. 6c. These coefficients, derived from fourth-order polynomial fittings, are listed in Table 2.a, Table 2.b, Table 2.c, and Table 2.d for the spinodal classes considered. The curves of Eq. (18) are fitted by a dataset of five porosity values ($\rho = [0.3, 0.4, 0.5, 0.6, 0.7]$) with

Table 2.a
Fitted curve coefficients c_s of isotropic spinodal class of the elastic material matrix homogenized $\mathbf{D}^H$.

D_{ij}^H	c_0	c_1	c_2	c_3	c_4
D_{11}^H	0.2523	−2.6095	8.5053	−8.9022	4.2839
D_{22}^H	0.2523	−2.6095	8.5053	−8.9022	4.2839
D_{33}^H	0.2523	−2.6095	8.5053	−8.9022	4.2839
D_{12}^H, D_{21}^H	0.0216	−0.3097	1.0693	−0.7977	0.5847
D_{13}^H, D_{31}^H	0.0216	−0.3097	1.0693	−0.7977	0.5847
D_{23}^H, D_{32}^H	0.0216	−0.3097	1.0693	−0.7977	0.5847
D_{44}^H	0.2523	−2.6095	8.5053	−8.9022	4.2839
D_{55}^H	0.2523	−2.6095	8.5053	−8.9022	4.2839
D_{66}^H	0.2523	−2.6095	8.5053	−8.9022	4.2839

Table 2.b
Fitted curve coefficients c_s of cubic spinodal class of the elastic material matrix homogenized $\mathbf{D}^H$.

D_{ij}^H	c_0	c_1	c_2	c_3	c_4
D_{11}^H	−0.5686	4.9495	−16.9580	28.3320	−15.5190
D_{22}^H	−0.5686	4.9495	−16.9580	28.3320	−15.5190
D_{33}^H	−0.5686	4.9495	−16.9580	28.3320	−15.5190
D_{12}^H, D_{21}^H	−0.1744	1.5640	−5.3845	8.5116	−4.2314
D_{13}^H, D_{31}^H	−0.1744	1.5640	−5.3845	8.5116	−4.2314
D_{23}^H, D_{32}^H	−0.1744	1.5604	−5.3845	8.5116	−4.2314
D_{44}^H	0.2246	−2.0260	6.2815	−7.5403	3.6424
D_{55}^H	0.2246	−2.0260	6.2815	−7.5403	3.6424
D_{66}^H	0.2246	−2.0260	6.2815	−7.5403	3.6424

bounds limit ensuring that the microstructure remains bi-continuous and to avoid isolated solids at low spinodal densities or enclosed voids at high spinodal densities. In this work, the represented curves in Fig. 6 are restricted according to manufacturability range $\rho = [0.4, 0.6]$, which allows the production of spinodal architectures by means of the water jetting powder-bed 3D printer technology, as shown in Section 3.1. In addition, the data points used for this extrapolation are represented by dots in Fig. 6c. Each data point represents the mean value of fifteen spinodal realizations for each non-zero component of the homogenized stiffness matrix $\mathbf{D}_m^H(\rho_\ell)$, $m = 1, \ldots, N^m$.
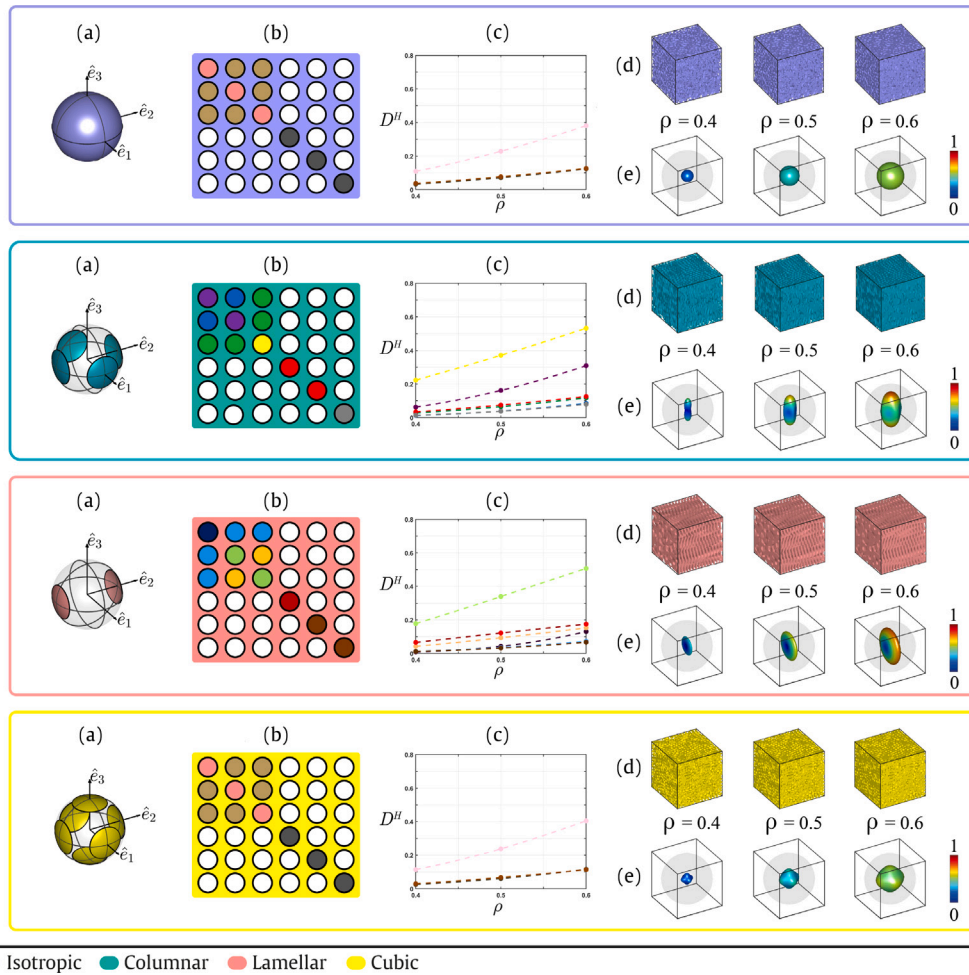
Fig. 6. Definition of spinodal architected materials classes: (a) wave vectors $\mathbf{n}_i$ space restricted by cone angles (θ_1, θ_2, θ_3). The spinodal material is defined by wave vectors belonging to the colored portion of the unit sphere surface; (b) components of the homogenized stiffness elasticity matrix, D^H, for each spinodal architected material, where colors are related to the values depicted in the interpolated value graph; (c) interpolated values of the elasticity matrix coefficients as a function of manufacturability range. Each dot represent mean value of fifteen spinodal topologies. The dashed lines represent fitted curves from polynomial interpolation; (d) examples of generated spinodal topologies with spinodal densities $\rho = 0.4$, 0.5, 0.6; (e) associated elastic surface of the generated spinodal architectures.

Table 2.c
Fitted curve coefficients c_s of lamellar spinodal class of the elastic material matrix homogenized $\mathbf{D}^H$.

D_{ij}^H	c_0	c_1	c_2	c_3	c_4
D_{11}^H	0.7404	−7.4228	25.0430	−30.5920	13.9840
D_{22}^H	−0.3344	3.1114	−10.2400	13.4090	−4.7212
D_{33}^H	0.7404	−7.4228	25.0430	−30.5920	13.9840
D_{12}^H, D_{21}^H	0.0881	−0.766	2.2924	−2.8458	1.8050
D_{13}^H, D_{31}^H	0.3646	−3.2923	10.2580	−12.4510	5.8646
D_{23}^H, D_{32}^H	0.0881	−0.766	2.2924	−2.8458	1.8050
D_{44}^H	−0.0088	0.1077	−0.5308	1.0760	−0.2344
D_{55}^H	−0.0088	0.1077	−0.5308	1.0760	−0.2344
D_{66}^H	0.3088	−3.0871	10.4910	−13.138	6.0157

Table 2.d
Fitted curve coefficients c_s of columnar spinodal class of the elastic material matrix homogenized $\mathbf{D}^H$.

D_{ij}^H	c_0	c_1	c_2	c_3	c_4
D_{11}^H	0.1439	−1.1318	2.2252	0.2854	−0.1390
D_{22}^H	−0.4462	2.5361	−4.2226	6.4342	−3.1826
D_{33}^H	0.1439	−1.1318	2.2252	0.2854	−0.1390
D_{12}^H, D_{21}^H	0.0744	−0.7230	2.2552	−2.422	1.452
D_{13}^H, D_{31}^H	−0.0144	0.1866	−0.9297	1.7814	−0.4921
D_{23}^H, D_{32}^H	0.0744	−0.723	2.2552	−2.422	1.452
D_{44}^H	0.0829	−0.7126	1.8308	−0.8956	0.0298
D_{55}^H	0.0829	−0.7126	1.8308	−0.8956	0.0298
D_{66}^H	−0.052	0.5379	−2.1236	3.638	−1.6457

3.3. Lamellar mapping and optimal material composition design of a catenary arch

Spinodal architected materials, as detailed in Section 3.2, have been employed to optimally allocate materials in an assigned domain. The proposed design approach aims at integrating artificial stone-like materials, produced by additive manufacturing, with a powerful computational optimization tool. The arch, in particular the catenary arch, represents an architectural element characterized by a thrust line, representing the theoretical path through which the resultants of compression forces pass, that is entirely contained within the shape of the arch. This theoretical concept has been implemented and exploited to design self-supported structures with optimized material distribution, porosity, and orientation. Material optimization is first performed on a catenary arch domain, where the design and boundary conditions are outlined in Fig. 7. Geometrically the axis of the arch has been defined by reversing the following equation:

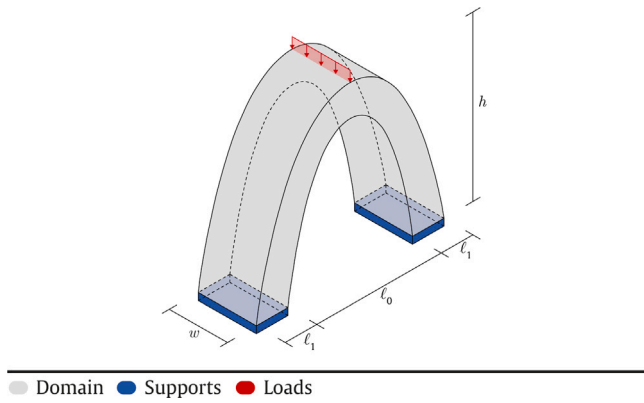$$z = d \cosh \frac{x}{d} = \frac{d}{2}(e^{\frac{x}{d}} + e^{-\frac{x}{d}}), \qquad (19)$$

● Domain   ● Supports   ● Loads

Fig. 7. Catenary arch: design domain and boundary conditions.

where d is a parameter which allows to control the scaling of the curve since all catenaries are similar to each other. The arch axis has been generated by setting $d = 1/6$ and solid arch volume has been defined by imposing constant depth along the axis, $\ell_1 = 15$ cm, with a span of $\ell_0 = 65$ cm. The overall length results $\ell = 95$ cm with an height of $h = 83$ cm and a width set as $w = 30$ cm. These geometrical dimensions allow to satisfy the geometric constraints imposed by the printer's envelope, where the maximum printable object has dimension of 1.5 m^3. The manufacturing process is tested to capture the spinodal features on a large-scale framework by mapping the lamellar spinodal architecture on the domain shown in Fig. 7.

In more detail, the implemented lamellar spindal material is defined by using Eq. (2), with restriction angles $(\theta_1, \theta_2, \theta_3) = (30°, 0°, 0°)$. The numerical model has been computed by fixing the spinodal density $\rho = 0.4$ on the whole domain, while the angle orientations (α, β, γ) follow the catenary axis. The model of the sample with the spinodal features of the mapped catenary arch is achieved through the post-processing strategy detailed in Section 2.4. The spinodal features, characterized by porosity and orientation parameters, were captured by setting the wavelength $\xi = 4$ cm^{-1} used to post-process the spinodal field. During the printing process, the arch was positioned horizontally, *i.e.* parallel to the laying and printing directions. This horizontal placement facilitated efficient printing, allowing the structure to be printed continuously along the entire printing direction, minimizing interruptions between layers. This approach aimed at reducing printing time, which is a crucial factor for a successful material activation, in order to set off the chemical reaction through selective deposition of the water-admixture solution. The printed structure is visually illustrated in Fig. 8, which highlights the scalability of the spinodal architectures with the design of a large-scale structure. The physical model has been printed making use of the materials and the technology described in Section 2.5.

The mapped catenary arch represented in Fig. 8 highlights an intrinsic problem of multi-scale modeling, in particular when a homogenization approach is adopted. Indeed, homogenization theory, relies on two main assumptions: infinite periodicity and adequate separation of length scales. Despite providing multiscale spatially variant solids with continuous connectivity and smooth transition between different spinodal architectures, these assumptions cannot be, in general, guaranteed. Indeed, despite the adoption of non-periodic spinodal architected materials that allow for smooth continuity between distinct spinodal classes, it is self-implied that infinite periodicity cannot be attained for non-periodic features. On the other hand, practical limitations in the manufacturing process may hinder the assumption of scale separation since, as a consequence of intrinsic 3D printer specifications – namely, maximum build volume and resolution – it is not practically possible to manufacture features at arbitrarily small scales, nor can the macrostructure be printed at an arbitrarily large scale. This

issue appears more evident in large-scale additive manufacturing with cement-based powder-bed technology, where the granular composition of aggregate imposes a limit in achieving high resolution. Thus, a possible strategy is to enlarge the printer build volume, which requires quite radical modifications in the manufacturing process [22]. Following up with these considerations, we propose the optimal designs of self-supported structures, which have been investigated by applying the *topology-by-material* optimization approach, as detailed in Section 2.2, to include non-periodic cell architectures in the assigned domain with optimal material distribution. The first numerical example presented was carried out on a catenary arch domain provided in Fig. 7, where the axis has been generated by setting $d = 1/6$, and the solid arch volume has been defined with a constant depth along the axis, $\ell_1 = 30$ cm, a width set as $w = 30$ cm and a span of $\ell_0 = 60$ cm. The full length is $\ell = 120$ cm and the height of arch is $h = 123$ cm. The load was applied on the tip of the arch crown, involving a uniform vertical load. In this case, a single global volume constraint, $\bar{v} \leq 0.4$, is considered in order to control the elements of the domain and the candidate materials. Here, the optimization of the input domain focuses on composition, porosity, and orientations. The geometric space and features are under full control with the global and local constraints. By setting an high global volume fraction, it becomes possible to fix the topology at the macro-scale thus preventing typical geometric features encountered in classical topology optimization, such as significant geometric shrinkage and void inclusion in the input domain. The optimization is performed by taking advantage of the symmetries of the domain. Thus, the studied domain is a quarter of the catenary arch, Fig. 7, which is discretized by hexahedral elements with regular edge of 0.0075 m. The catenary arch is designed considering the four implemented spinodal classes detailed in Fig. 6 with a density range $0.4 \leq \rho \leq 0.6$, imposed by manufacturability constraints. Also, the orientation angles, α, β, γ, are allowed to vary freely in the range $[-\pi, \pi]$, whose domain is equivalent to a circle through modular arithmetic of 2π. The optimization parameters are detailed in Section 3.5.

In the numerical simulation performed, the optimal design entails the presence of a single-material columnar spinodal architecture. The optimal design with spinodal features is shown in Fig. 9. Columnar spinodal architecture exhibits a dominant vertical strength direction, as depicted by the elastic surface in Fig. 6e. Moreover, the material aligns itself along the principal stress direction, as shown by the frontal view section in Fig. 9b. The orientation angles alignment is consistent with observations highlighted by the pioneering work by Michell on topology optimization [55]. Spinodal density, illustrated in Fig. 10, exhibits high values along the orientation streamlines of the catenary arch (Fig. 9b). Consequently, these regions are characterized by low porosity.

Low porosity indicates stiffer regions, which is coherent with the optimal alignment of the microstructure in order to bear the applied load. The opposite can be observed near the boundary of the layout, such as the extrados and intrados of the arch. This ensures the consistency of the approach in accurately representing spinodal features with an adequate length scale according to the printer's resolution.

3.4. Optimal material composition design of catenary groin vault

Three numerical examples are illustrated in the present section to optimize and design a lightweight catenary groin vault, which is given by the intersection of two catenary barrel vaults with a width $\ell = 150$ cm and ledges $\ell_2 = 15$ cm. The height of the groin vault is 123 cm. Depth and span are set constant, respectively of $\ell_1 = 30$ cm and $\ell_0 = 60$ cm. The piers at the bottom are fixed, while a unitary uniform distributed load is applied at the extrados of the longitudinal and transversal ridge ribs. The full domain is provided in Fig. 11, while the simulations are performed on a quarter domain exploiting the symmetry with respect to the *x-y* Cartesian axes. The domain is discretized with hexahedral elements with edge length of 0.01 m.
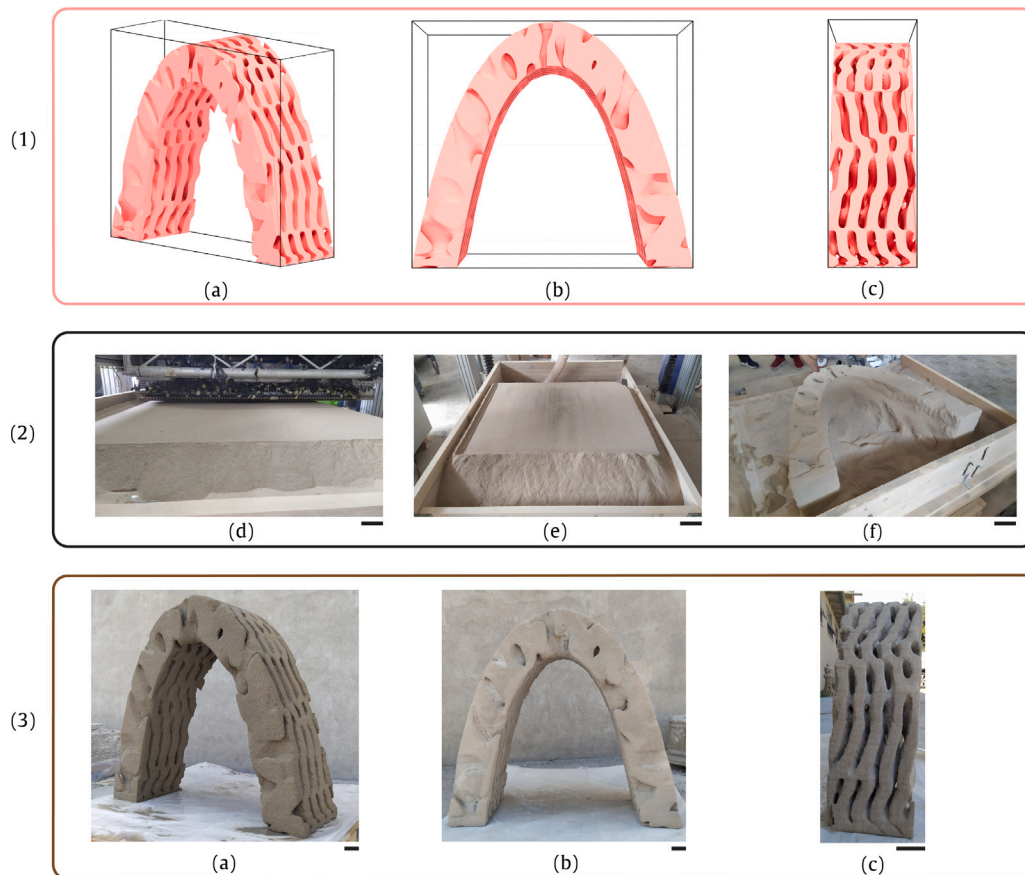
Fig. 8. Catenary arch mapped by a lamellar spinodal architected material: (1) numerical model with (a) isometric view, (b) frontal view, (c) lateral view; (2) printing process with (d) layer printing, (e) final layer, (f) post-processing; (3) physical model. The scale bars at the bottom-right corner of each image represent 10 cm.
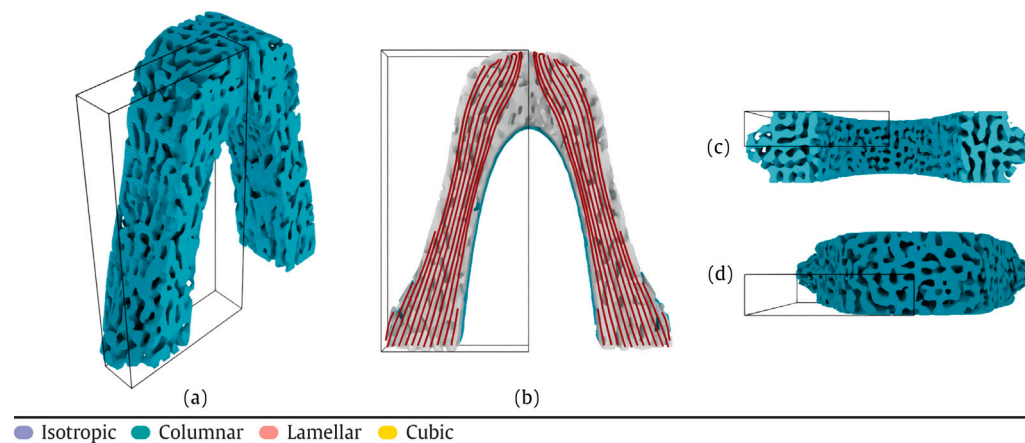

● Isotropic   ● Columnar   ● Lamellar   ● Cubic

Fig. 9. Material distribution of spinodal columnar catenary arch: (a) isometric view; (b) frontal view with section highlighting the material orientation streamlines; (c) bottom view; (d) top view.

The first numerical example on the catenary groin vault aims at capturing the optimal material distribution in terms of orientation and porosity for a single candidate material, represented by the columnar spinodal architecture, as depicted in Fig. 12. In this case, the selection of the material has been informed by the multi-material optimization of the catenary arch, discussed in the previous subsection. The selected material has been optimally distributed and oriented inside the assigned domain with a single global constraint on the overall volume fraction $\bar{v}$.

The maximum stiffness axis of the columnar material is aligned along the axis of the vault in the direction of the load applied on the tip,

as shown in Fig. 11b. The orientation and density distribution exhibit a similar pattern to that observed in the columnar catenary arch (see Section 3.3), where both indicate lower porosity in the inner regions of the domain. In these areas, the piers of the groin vault (see Fig. 13) experience higher stress and bear the applied load of the structure. This distribution suggests that regions with higher porosity, *i.e.* lower density, allow for a reduction in overall weight, thereby improving structural efficiency.

The second example, shown in Fig. 14, explores the *topology-by-material* optimization approach in a multi-material setting, which considers the four main classes of spinodal architectures (isotropic, cubic,
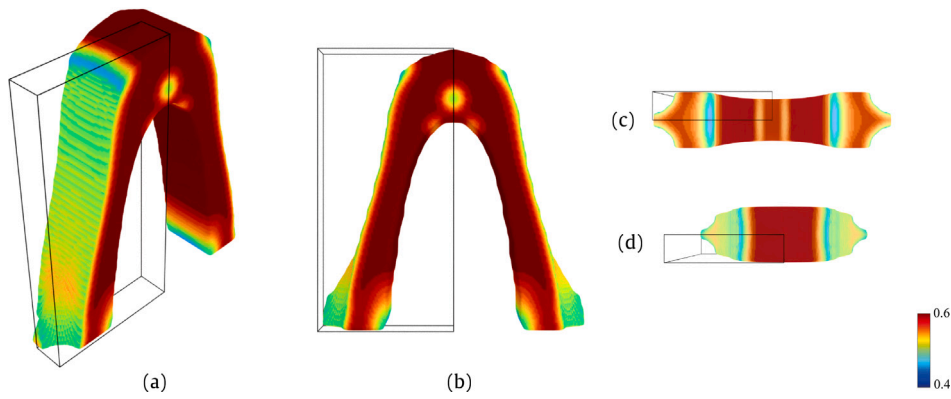
Fig. 10. Density distribution in the spinodal columnar catenary arch: (a) isometric view; (b) frontal view; (c) bottom view; (d) top view.
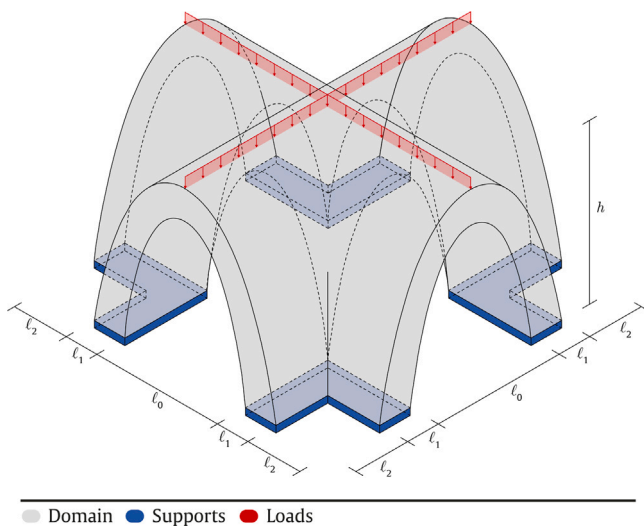

Domain ● Supports ● Loads

Fig. 11. Catenary groin vault: design domain and boundary conditions.

directions. This numerical result represents a local optimal minimum, where the difference between the compliance of the multi-material groin vault, f_m, is close to the one of the single-material groin vault, f_0. These results demonstrate that increasing the material design space does not necessarily result in structures with higher performance. On the contrary, the restriction of the design freedom with local constraints by forcing the presence of multiple materials leads to less performant designs [43].

The last numerical example is carried out considering four local volume constraints. In this case, the constraints are used to control the material distribution of the domain such that the composition of each candidate material is limited to the 25%, i.e. $\overline{v}_j = 0.25\overline{v}, j = 1, \dots, 4$, of the global volume fraction, $\overline{v} = 0.4$.

The numerical result with local constraints, as illustrated in Fig. 15, shows evidences of an optimal solution with a lower mechanical performance as depicted by the convergence graph of compliance over iteration shown in Fig. 16, where the material distribution has a more elaborated layout to guarantee the presence of all the candidate materials. Isotropic and cubic materials are placed in regions aimed at distributing the load to the piers, while lamellar and columnar materials are prevailing in areas where preferential strength directions are required, such as the piers.

3.5. Topology-by-material optimization algorithmic parameters and computational resources

The design variables are initialized by an initial guess, which satisfies both the local and global volume constraints applied. In particular, each spinodal material has an equal volume ($v_{lm} = \overline{v}/\rho_\ell, \forall_\ell$), density ($\rho_\ell = (\underline{\rho} + \overline{\rho})/2, \forall_\ell$) and angle ($\alpha_\ell = 0, \beta_\ell = 0, \gamma_\ell = 0, \forall_\ell$). Design variables are filtered by a linear filter with a given radius, R. During each iteration, the design variables are updated according to a suitable update solution scheme (see Section 2.3). The convergence is assessed by evaluating the change in material density, $\mathbf{Z}$, within a given tolerance, tol, or when the maximum number of iterations max_{iter} is reached for each penalization step. The density, Z, for each material is updated according to a move limit, mv_Z, as are the orientation design variables, α, β, γ, by mv_{angle}. The optimal solution is sought through a continuation penalization scheme, achieved by conducting 5 penalization steps. In each step, both the material interpolation penalty parameter, denoted as p, and the multi-material interpolation parameter, represented by τ, are updated. Once the penalization steps are completed, Heaviside projection is employed to eliminate mixing regions. Heaviside projection parameters are comprehensive of the threshold η, which remains fixed for all the iterations, while the sharpness of the approximation κ is progressively increased with 200 iterations, denoted as κ_{iter}, with the formula $\kappa_{i+1} = 1.25\kappa_i + 0.5$ until reaching the maximum assigned value,

lamellar, and columnar). We highlight that, although the optimizer is free to utilize the four candidate materials in any proportion, the final optimized structure only has columnar and lamellar materials. This choice of materials stems from the optimization process itself, as the aforementioned materials lead to a more efficient design.

The materials selected through the iterative process exhibit distinct preferred strength directions, as depicted by the elastic surfaces in Fig. 6. Specifically, the lamellar class exhibits two main strength directions, with lower stiffness perpendicular to these directions, while the columnar shows a dominant strength direction, with lower stiffness in other directions but consistent behavior across the perpendicular plane to the main strength. Based on these materials definition it is possible to explain the material placement in Fig. 14. Indeed, the lamellar material is located as continuous connection between the transversal and longitudinal ridge rib, where the load is applied, and the groin vault piers. Here, the vertical loads are transferred to the piers through the lamellar band nearby the intrados tip of the vaults, which crosses the whole panels. An explanation of this specific material location could be found in the material properties of the lamellar spinodal class, where a double high strength direction helps the distribution of stress on the vertical columnar panels and faces the multiple load
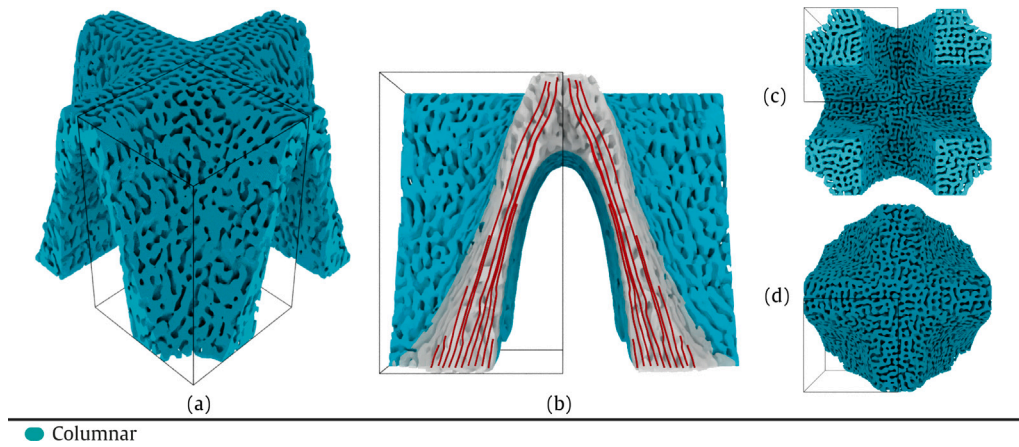
Fig. 12. Material distribution of columnar catenary groin vault: (a) isometric view; (b) frontal view with section highlighting the material orientation streamlines; (c) bottom view; (d) top view.
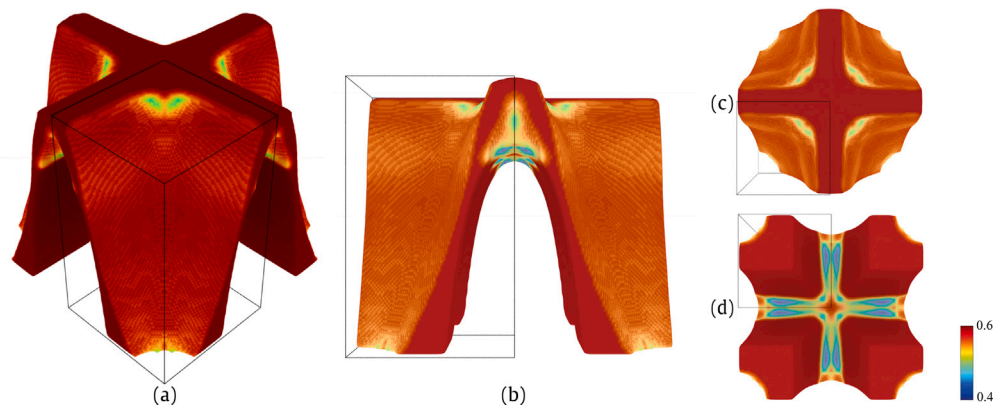

Fig. 13. Density distribution for the columnar catenary groin vault: (a) isometric view; (b) frontal view; (c) bottom view; (d) top view.
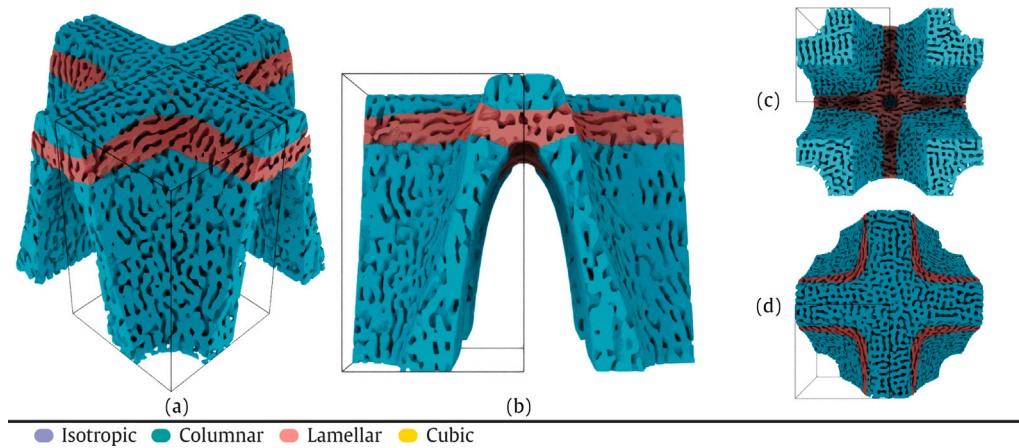

Fig. 14. Material distribution of the multi-material catenary groin vault: (a) isometric view; (b) frontal view; (c) bottom view; (d) top view.

κ_{max}. The detailed parameters are reported in Table 3. The numerical solutions[1] are obtained by solving a quarter of the domain, *i.e.* the symmetry is enforced at the centerline of the arches and groin vaults along the symmetry axes, parallel to the plane $x - z$ and $y - z$.

---

[1] All numerical tests have been performed on a machine with 24 Intel Xeon CPUs, 251 GB of RAM, and NVIDIA Titan Xp GPUs with 12 GB of RAM.

4. Discussion

Spinodal architected materials, characterized by their tunable stiffness properties, have been embedded into self-supported structures using a methodology that encompasses both the manufacturing process and a novel optimization formulation. The manufacturing process has been thoroughly described, including the actual printing of several samples. These include cubes constructed from different spinodal architected materials, as well as a lamellar spinodal catenary arch. The
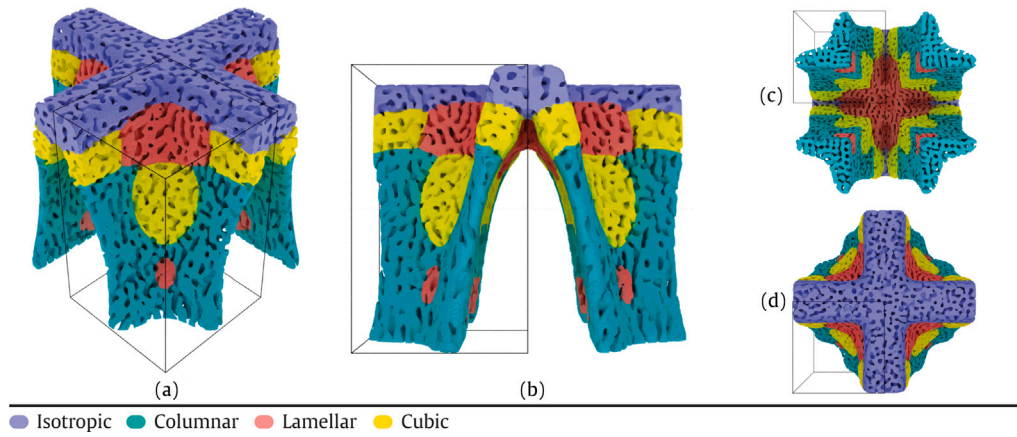
Fig. 15. Material distribution of the multi-material catenary groin vault with local constraints: (a) isometric view; (b) frontal view; (c) bottom view; (d) top view.

Table 3
Numerical parameters adopted in the optimization.

| Parameter	Description	Optimization values
p	SIMP penalization factor	[1 2 2 3 4]
τ	multi-material penalization factor	[0 0.2 0.4 0.7 1]
q	Filter exponent	1
R	Filter radius	0.4
κ_{init}	Sharpness Heaviside Projection	0.1
κ_{iter}	Iter update sharpness Heaviside Projection	30
κ_{max}	Max value of sharpness Heaviside Projection	15
η	Threshold Heaviside Projection	0.5
λ	Initial augmented lagrangian multiplier	0
μ	Initial augmented lagrangian penalization	1
ι	Initial augmented lagrangian step size	1
max_{iter}	Maximum iterations	[100 100 100 100 100]
tol	Convergence tolerance	0.02
$mv_{(Z)}$	Optimization material density move limit	0.1
$mv_{(\alpha,\beta,\gamma)}$	Optimization orientation move limit	0.25
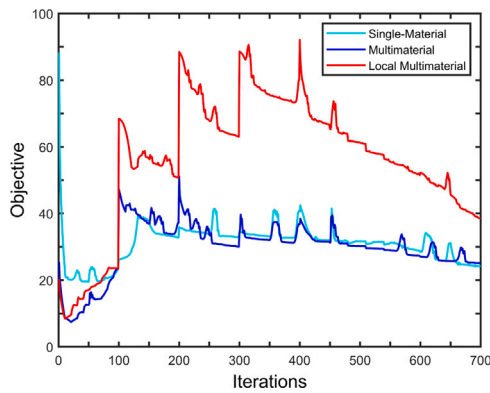
Fig. 16. Convergence plot for the catenary groin vault with global constraints, in both single-material and multi-material frameworks, and local constraints.

physical models allowed to capture details and features of the printer, enabling the development and illustration of a strategic approach to address challenges related to the structural optimization of 3D printed large-scale structures composed of materials with negligible tensile strength. We tailored a *topology-by-material* approach to seek numerically optimal layouts of self-supported structures (*e.g.* catenary arch and groin vault). The topological macro-scale space does not involve changes by carefully setting optimization parameters, such as the global volume fraction and spinodal density range, while at the micro-scale the topological space is optimized by a suitable distribution of spinodal architectures. This allows to preserve the prevalent compression state

of self-supported structures, which are the input domain of our optimization results, see Section 3. Additionally, this approach leverages on local volume constraints to enhance the stiffness properties of a given design. The structural optimization problem is solved by minimizing compliance to achieve high-performance designs. Additionally, the optimization approach explores the design space of candidate materials, which allows free-variations in material orientations and porosity distribution, while different non-periodic spinodal microstructures with isotropic and anisotropic properties are included.

The introduction of a volume fraction, which limits the formation of voids, allows to address the challenge of optimizing large-scale structures, even in the case of self supporting structures made of stone-like materials exhibiting negligible tensile strength. Notably, the printed samples emphasize the importance of safeguarding the continuity of the structure, *i.e.* preserving the topology of the assigned domain. The voids, in terms of porosity, are implicitly included to design hierarchical structures by means of microstructures with inner stochastic void distribution, set by manipulating the GRF of the spinodal architectures. This consideration is particularly relevant in light of the presence of voids dictated by classical topology optimization, which could lead to truss-like or shell-like solutions. In such cases, structures experience areas of tension and compression at the macro-scale. To address this, it is essential to limit the formation of gaps and cavities, focusing the optimization on geometry. The optimized layouts leverage symmetry properties of the domain and boundary conditions to reduce the computational cost. Here, the linearity of the material and the objective function further contributes to symmetry in the optimized structures. We point out that other topology optimization formulations, such as stress-based formulations [38,56,57], might lead to non-symmetric results. Our present formulation is compliance-based

and does not include any strength or failure criteria.

The multi-material optimization includes different spinodal architected material classes. It is known in multi-material structures that issues due to weak interfaces emerge between dissimilar materials, both in multi-material topology optimization [22] and in multi-material 3D printing [58]. In this work, the formation of weak interfacial connections between distinct materials is prevented by adopting a post processing technique which involves the interpolation of the phase field representation of spinodal microstructures as described in Section 2.4. We also point out that the additive manufacturing process is entirely carried out by using a single printing material for the whole sample.

Furthermore, the choice of non-periodic architected materials facilitates the design of well-connected structures with smoothed continuity between different materials. Unlike truss-based lattice structural systems, which exhibit high-stress concentrations at junctions, the use of double curvature surfaces, similarly to the Triply Periodic Minimal Surface (TPMS) with nearly zero mean curvature [59], and the doubly curved solid architectures, avoid irregular connections accomplishing high stiffness on the surfaces [60]. Supported by these observations, we explore the optimal design of self-supported structures by suggesting designs with optimal material distribution, porosity and orientations according to the imposed domain and boundary conditions. Additionally, the printed samples demonstrate the scalability of additively manufactured spinodal architectures, in particular in the context of the presented powder-bed water-jet 3D printing technology.

5. Conclusions

In this paper we tailor a new design methodology for optimal 3D printed hierarchical self supporting structures, manufactured in synergy with an innovative water-jet powder-bed additive manufacturing technology. Here, spinodal architected materials are adopted and scaled-up through large-scale additive manufacturing. Within this framework, the proposed methodology aims at harnessing the high design freedom provided by additive manufacturing and bridging the additive manufacturing processes of large-scale hierarchical structures with a new multi-scale and multi-material topology optimization approach, denoted as *topology-by-material*. We address the challenges of large-scale additive manufacturing by presenting 3D printed samples using concrete-like materials with negligible tensile strength and suggesting optimal designs derived from the proposed topology optimization formulation. The physical samples demonstrate the scalability of spinodal architectures, as well as their integration with complex domains.

Future research directions encompass the inclusion of worst-case load scenarios, *i.e.* the case of continuously varying load directions and magnitudes and real-world actions, *i.e.* wind and seismic loads. Additionally, the generalization of the formulation in the presence of stress constraints will allow to impose a failure criterion at the microscale which could significantly expand the application range and the efficiency of additive manufacturing techniques in the field of civil engineering.

CRediT authorship contribution statement

Andrea Nale: Writing – review & editing, Writing – original draft, Investigation, Formal analysis, Data curation, Conceptualization. **Andrea Chiozzi:** Writing – review & editing, Writing – original draft, Supervision, Resources, Project administration, Methodology, Investigation, Funding acquisition, Formal analysis, Conceptualization. **Fernando V. Senhora:** Visualization, Validation, Software, Formal analysis, Data curation, Conceptualization. **Glaucio H. Paulino:** Writing – review & editing, Supervision, Resources, Methodology, Conceptualization.

Declaration of competing interest

The authors declare that they have no known competing financial interests or personal relationships that could have appeared to influence the work reported in this paper.

Acknowledgments

Appendix A. Stress transformation rotational matrix

This section presents the stress transformation rotational matrix used to rotate the reference frame of the microstructures:

$$\mathbf{M} = \begin{bmatrix} A & B \\ C & D \end{bmatrix}, \tag{A.1}$$

which is defined by the following matrix:

$$\mathbf{A} = \begin{bmatrix} R_{11}^2 & R_{12}^2 & R_{13}^2 \\ R_{21}^2 & R_{22}^2 & R_{23}^2 \\ R_{31}^2 & R_{32}^2 & R_{33}^2 \end{bmatrix}, \tag{A.2a}$$

$$\mathbf{B} = \begin{bmatrix} 2R_{12}R_{13} & 2R_{13}R_{11} & 2R_{11}R_{12} \\ 2R_{22}R_{23} & 2R_{23}R_{21} & 2R_{21}R_{22} \\ 2R_{32}R_{33} & 2R_{33}R_{31} & 2R_{31}R_{33} \end{bmatrix}, \tag{A.2b}$$

$$\mathbf{C} = \begin{bmatrix} R_{21}R_{31} & R_{22}R_{32} & R_{23}R_{33} \\ R_{31}R_{11} & R_{32}R_{12} & R_{33}R_{13} \\ R_{11}R_{21} & R_{12}R_{22} & R_{13}R_{23} \end{bmatrix}, \tag{A.2c}$$

$$\mathbf{D} = \begin{bmatrix} R_{22}R_{33} + R_{23}R_{32} & R_{21}R_{33} + R_{23}R_{31} & R_{22}R_{31} + R_{21}R_{32} \\ R_{12}R_{33} + R_{13}R_{32} & R_{13}R_{31} + R_{11}R_{33} & R_{11}R_{32} + R_{12}R_{31} \\ R_{12}R_{23} + R_{13}R_{22} & R_{13}R_{21} + R_{11}R_{23} & R_{11}R_{22} + R_{12}R_{21} \end{bmatrix}, \tag{A.2d}$$

where each component of the rotation matrix $\mathbf{R}$ is computed by the product of three orthogonal matrix of the angles α, β, γ associated to the x_3, x_2, x_1 axes:

$$\mathbf{R} = \begin{bmatrix} c_\beta c_\alpha & c_\beta s_\alpha & s_\beta \\ -s_\gamma s_\beta c\alpha - c_\gamma s_\alpha & -s_\alpha s_\gamma s_\beta + c_\gamma c_\alpha & s_\gamma c_\beta \\ -c_\alpha c_\gamma s_\beta + s_\alpha s_\gamma & -s_\alpha c_\gamma s_\beta - s_\gamma c_\beta & c_\gamma c_\beta \end{bmatrix}, \tag{A.3}$$

where $c_{(\cdot)}$ $s_{(\cdot)}$ respectively denote the cosine and sine of the angles α, β, γ about the three orthogonal axes. Finally, the interpolation function penalizes the mixing through a multi-material interpolation factor τ.

Appendix B. Sensitivity analysis

In this section, we derive the sensitivities employed to update the design variables. Indeed, the optimization problem is solved by a gradient-based optimization algorithm Section 2.3, and hence it is necessary to provide the sensitivity information. The sensitivities of the

objective and constraint functions with respect to each design variable are calculated as follows:

$$\frac{\partial f}{\partial \mathbf{z}_m} = \frac{\partial y_{\ell m}}{\partial z_{\ell m}} \frac{\partial \tilde{y}_{\ell m}}{\partial y_{\ell m}} \frac{\partial f}{\partial w_{\ell m}}, \quad \frac{\partial f}{\partial \boldsymbol{\alpha}_m} = \frac{\partial f}{\partial \alpha_{\ell m}},$$

$$\frac{\partial f}{\partial \boldsymbol{\beta}_m} = \frac{\partial f}{\partial \beta_{\ell m}}, \quad \frac{\partial f}{\partial \boldsymbol{\gamma}_m} = \frac{\partial f}{\partial \gamma_{\ell m}}, \quad \frac{\partial f}{\partial \rho} = \frac{\partial f}{\partial \rho_{\ell}}$$

$$\frac{\partial g_j}{\partial \mathbf{z}_m} = \frac{\partial y_{\ell m}}{\partial z_{\ell m}} \frac{\partial \tilde{y}_{\ell m}}{\partial y_{\ell m}} \frac{\partial v_{\ell m}}{\partial \tilde{y}_{\ell m}} \frac{\partial g_j}{\partial v_{\ell m}}, \quad \frac{\partial g_j}{\partial \boldsymbol{\rho}} = \frac{\partial v_{\ell m}}{\partial \rho_{\ell}} \frac{\partial g_j}{\partial v_{\ell m}},$$

$$m = 1, \dots, N^m, \quad j = 1, \dots, N^c$$

$$(B.1)$$

where $\frac{\partial \mathbf{y}_m}{\partial \mathbf{z_m}} = \mathbf{P}^T$.

The components of each objective and constraint sensitivities are defined as:

$$\frac{\partial f}{\partial w_{\ell m}} = -\mathbf{U}^T \frac{\partial \mathbf{K}}{\partial w_{\ell m}} \mathbf{U}, \quad \frac{\partial f}{\partial \rho_{\ell}} = -\mathbf{U}^T \frac{\partial \mathbf{K}}{\partial \rho_{\ell}} \mathbf{U},$$

$$\frac{\partial f}{\partial \alpha_{\ell m}} = -\mathbf{U}^T \frac{\partial \mathbf{K}}{\partial \alpha_{\ell m}} \mathbf{U}, \quad \frac{\partial f}{\partial \beta_{\ell m}} = -\mathbf{U}^T \frac{\partial \mathbf{K}}{\partial \beta_{\ell m}} \mathbf{U}, \quad \frac{\partial f}{\partial \gamma_{\ell m}} = -\mathbf{U}^T \frac{\partial \mathbf{K}}{\partial \gamma_{\ell m}} \mathbf{U},$$

$$\frac{\partial w_{kr}}{\partial \tilde{y}_{\ell m}} = \begin{cases} p y_{\ell m}^{p-1}, & \text{if } l = k \text{ and } r = m \\ 0, & \text{otherwise} \end{cases}$$

$$\frac{\partial \tilde{y}_{kr}}{\partial y_{\ell m}} = \begin{cases} \frac{\xi(1 - \tanh^2(\xi(y_{\ell m} - \eta)))}{\tanh(\xi\eta) + \tanh(\xi(1-\eta))}, & \text{if } l = k \text{ and } r = m \\ 0, & \text{otherwise} \end{cases}$$

$$(B.2)$$

$$\frac{\partial v_{\ell m}}{\partial \tilde{y}_{rk}} = \begin{cases} \rho_{\ell}, & \text{if } l = k \text{ and } r = m \\ 0, & \text{otherwise} \end{cases}$$

$$\frac{\partial v_{\ell m}}{\partial \rho_k} = \begin{cases} \tilde{y}_{\ell m}, & \text{if } \ell = k \\ 0, & \text{otherwise} \end{cases}$$

$$\frac{\partial g_j}{\partial v_{\ell m}} = \frac{V_{\ell}}{\sum_{\ell \in E_j} V_{\ell}},$$

where the stiffness sensitivities are computed from the material elasticity tensor, defined in Eq. (10), with respect to the design variable **w**:

$$\frac{\partial \mathbf{D}_k}{\partial w_{\ell m}} = \begin{cases} \prod_{\substack{q=1 \\ q \neq m}}^{N^m} (1 - \tilde{\gamma} w_{\ell q}) \mathbf{M}_k \mathbf{D}_m^H(\rho_\ell) \mathbf{M}_k^T + \\ - \sum_{\substack{q=1 \\ q \neq m}}^{N^m} \gamma w_{\ell q} \prod_{\substack{r=1 \\ r \neq q \\ r \neq m}}^{N^m} (\tilde{\gamma}_{\ell r}) \mathbf{M}_k \mathbf{D}_m^H(\rho_\ell) \mathbf{M}_k^T, & \text{if } \ell = k \\ \\ 0, & \text{otherwise} \end{cases}$$

$$(B.3)$$

and with respect to the density, ρ, and the orientations, $(\boldsymbol{\alpha}, \boldsymbol{\beta}, \boldsymbol{\gamma})$:

$$\frac{\partial \mathbf{D}_k}{\partial \rho_\ell} = \begin{cases} \sum_{m=1}^{N^m} w_{\ell m} \prod_{\substack{q=1 \\ q \neq m}}^{m} (1 - \tilde{\gamma} w_{\ell q}) \mathbf{M}_k \frac{\partial \mathbf{D}_m^H(\rho_k)}{\partial \rho_\ell} \mathbf{M}_k^T & \text{if } \ell = k \\ & \frac{(\partial \mathbf{D}_m^H)_{qs}}{\rho_\ell} = \frac{(\partial \mathcal{F}_m)_{qs}}{\rho_\ell} \\ 0, & \text{otherwise} \end{cases}$$

$$(B.4)$$

$$\frac{\partial \mathbf{D}_k}{\partial \alpha_{\ell m}} = \begin{cases} \sum_{m=1}^{N^m} w_{\ell m} \prod_{\substack{q=1 \\ q \neq m}}^{N^m} (1 - \tilde{\gamma} w_{\ell q}) [\frac{\partial \mathbf{M}_k}{\partial \alpha_{\ell m}} \mathbf{D}_m^H \mathbf{M}_k^T + \mathbf{M}_k \mathbf{D}_m^H \frac{\partial \mathbf{M}_k^T}{\partial \alpha_{\ell m}}] & \text{if } \ell = k \\ 0, & \text{otherwise} \end{cases}$$

$$(B.5)$$

$$\frac{\partial \mathbf{D}_k}{\partial \beta_{\ell m}} = \begin{cases} \sum_{m=1}^{N^m} w_{\ell m} \prod_{\substack{q=1 \\ q \neq m}}^{N^m} (1 - \tilde{\gamma} w_{\ell q}) [\frac{\partial \mathbf{M}_k}{\partial \beta_{\ell m}} \mathbf{D}_m^H \mathbf{M}_k^T + \mathbf{M}_k \mathbf{D}_m^H \frac{\partial \mathbf{M}_k^T}{\partial \beta_{\ell m}}] & \text{if } \ell = k \\ 0, & \text{otherwise} \end{cases}$$

$$(B.6)$$

Table C.1
Nomenclature for spinodal architected materials, optimization algorithm and numerical post-processing.

Symbol	Description
Spinodal Architected Material	
ψ	Gauss Random Field (GRF)
$\mathbf{n}_i$	Wave vectors
$\hat{\mathbf{e}}_1, \hat{\mathbf{e}}_2, \hat{\mathbf{e}}_3$	Cartesian basis in $\mathbb{R}^3$
$\theta_1, \theta_2, \theta_3$	
ω_i	Phase shift
ξ	Wavelength
ψ_{cut}	Level-set Threshold
Topology-by-material Optimization	
f	Compliance
g	Volume Constraint
$\mathbf{F}$	Force vector
$\mathbf{U}$	Displacement field
$\mathbf{K}$	Global stiffness matrix
$\mathbf{B}$	Element-strain displacement matrix
V	Global stiffness matrix
$\mathcal{G}_j$	Indices of materials associated to local constraints j
$\mathcal{E}_j$	Indices of elements associated to local constraints j
$\mathbf{x}$	Coordinate centroids of elements
$\mathbf{Z}$	Material density
$\mathbf{Y}$	SIMP interpolation of filtered material density
$\mathbf{W}$	Heaviside projection of material density
α, β, γ	Orientation of reference frame (x_1, x_2, x_3)
ρ	Spinodal density
p	SIMP penalization factor
τ	Multi-material penalization factor
R	Filter radius
q	Filter exponent
λ	Augmented lagrangian multiplier
μ	Augmented lagrangian penalization
ι	Augmented lagrangian step size
κ	Sharpness of the Heaviside Projection function
η	Threshold of the Heaviside Projection function
$\max_{\text{iter}}$	Maximum iterations
tol	Convergence tolerance
$mv_{(Z)}$	Optimization material density move limit
$mv_{(\alpha, \beta, \gamma)}$	Optimization orientation move limit
Post-Processing	
$\mathcal{B}$	Sets of candidate materials
$\boldsymbol{\psi}^0$	Projected Gauss Random Field
$\tilde{\mathbf{x}}$	Coordinate centroids of voxels
$\tilde{\mathbf{Z}}$	Projected material density
$\tilde{\mathbf{Y}}$	SIMP interpolation of filtered projected material density
$\tilde{\alpha}, \tilde{\beta}, \tilde{\gamma}$	Projected orientations of reference frame (x_1, x_2, x_3)
$\tilde{\rho}$	Projected spinodal architected material density
R_ψ	Radius of interpolated GRF field
Generic Nomenclature	
N^w	Number of wave vectors
N^c	Number of volume constraints
N^v	Number of voxels
N^e	Number of elements
N^m	Number of microstructures

$$\frac{\partial \mathbf{D}_k}{\partial \gamma_{\ell m}} = \begin{cases} \sum_{m=1}^{N^m} w_{\ell m} \prod_{\substack{q=1 \\ q \neq m}}^{N^m} (1 - \tilde{\gamma} w_{\ell q}) [\frac{\partial \mathbf{M}_k}{\partial \gamma_{\ell m}} \mathbf{D}_m^H \mathbf{M}_k^T + \mathbf{M}_k \mathbf{D}_m^H \frac{\partial \mathbf{M}_k^T}{\partial \gamma_{\ell m}}] & \text{if } \ell = k \\ 0, & \text{otherwise} \end{cases}$$

$$(B.7)$$

Finally, the sensitivities are substituted in the augmented lagrangian function (Eq. (11)):

$$\frac{\partial \mathcal{L}(\mathbf{x})^{(\mathbf{t})}}{\partial \mathbf{x}} = \frac{\partial f(\mathbf{x})}{\partial \mathbf{x}} + \sum_{j=1}^{K} [\lambda_j^{(t)} \max(\frac{\partial g_j(x)}{\partial \mathbf{x}}, -\frac{\lambda_j^{(t)}}{\mu^{(t)}})$$

$$+ \frac{\mu^{(t)}}{2} \max(\frac{\partial g_j(x)}{\partial \mathbf{x}}, -\frac{\lambda_j^{(t)}}{\mu^{(t)}})^2]$$

$$(B.8)$$

Appendix C. Nomenclature

See Table C.1.

Data availability

Data will be made available on request.

References

[1] S. Adriaenssens, P. Block, D. Veenendaal, C. Williams, Shell Structures for Architecture: Form Finding and Optimization, Routledge, 2014.

[2] T.E. Boothby, Analysis of masonry arches and vaults, Prog. Struct. Eng. Mater. 3 (3) (2001) 246–256.

[3] L.C. Lancaster, Concrete Vaulted Construction in Imperial Rome: Innovations in Context, Cambridge University Press, 2005.

[4] S. Huerta, Structural design in the work of gaudi, Archit. Sci. Rev. 49 (4) (2006) 324–339.

[5] A. Paolini, S. Kollmannsberger, E. Rank, Additive manufacturing in construction: A review on processes, applications, and digital planning methods, Addit. Manuf. 30 (2019) 100894.

[6] M. Javaid, A. Haleem, R.P. Singh, R. Suman, S. Rab, Role of additive manufacturing applications towards environmental sustainability, Adv. Ind. Eng. Polym. Res. 4 (4) (2021) 312–322.

[7] S. Lim, R.A. Buswell, T.T. Le, S.A. Austin, A.G. Gibb, T. Thorpe, Developments in construction-scale additive manufacturing processes, Autom. Constr. 21 (2012) 262–268.

[8] S. Ford, M. Despeisse, Additive manufacturing and sustainability: an exploratory study of the advantages and challenges, J. Clean. Prod. 137 (2016) 1573–1587.

[9] H. Hegab, N. Khanna, N. Monib, A. Salem, Design for sustainable additive manufacturing: A review, Sustain. Mater. Technol. (2023) e00576.

[10] M.P. Bendsoe, O. Sigmund, Topology Optimization: Theory, Methods, and Applications, Springer Science & Business Media, 2003.

[11] J. Wu, O. Sigmund, J.P. Groen, Topology optimization of multi-scale structures: a review, Struct. Multidiscip. Optim. 63 (2021) 1455–1480.

[12] M.P. Bendsøe, N. Kikuchi, Generating optimal topologies in structural design using a homogenization method, Comput. Methods Appl. Mech. Engrg. 71 (2) (1988) 197–224.

[13] A. Heyde, L. Guo, C. Jost, G. Theraulaz, L. Mahadevan, Self-organized biotectonics of termite nests, Proc. Natl. Acad. Sci. 118 (5) (2021) e2006985118.

[14] J. Huang, L. Gibson, Microstructural design of cellular materials—i: honeycomb beams and plates, Acta Met. Mater. 43 (4) (1995) 1643–1650.

[15] Y. Mistry, O. Weeger, S. Morankar, M. Shinde, S. Liu, N. Chawla, X. Chen, C.A. Penick, D. Bhate, Bio-inspired selective nodal decoupling for ultra-compliant interwoven lattices, Commun. Mater. 4 (1) (2023) 35.

[16] T. Maconachie, M. Leary, B. Lozanovski, X. Zhang, M. Qian, O. Faruque, M. Brandt, Slm lattice structures: Properties, performance, applications and challenges, Mater. Des. 183 (2019) 108137.

[17] T. Tancogne-Dejean, M. Diamantopoulou, M.B. Gorji, C. Bonatti, D. Mohr, 3D plate-lattices: an emerging class of low-density metamaterial exhibiting optimal isotropic stiffness, Adv. Mater. 30 (45) (2018) 1803334.

[18] M. Sam, R. Jojith, N. Radhika, Progression in manufacturing of functionally graded materials and impact of thermal treatment—a critical review, J. Manuf. Process. 68 (2021) 1339–1377.

[19] D. Shidid, M. Leary, P. Choong, M. Brandt, Just-in-time design and additive manufacture of patient-specific medical implants, Phys. Procedia 83 (2016) 4–14.

[20] Z. Hao, X. Zhang, Z. Huizhong, Y. Huning, L. Hongshuai, L. Xiao, W. Yaobing, Lightweight structure of a phase-change thermal controller based on lattice cells manufactured by slm, Chin. J. Aeronaut. 32 (7) (2019) 1727–1732.

[21] Z. Du, X.-Y. Zhou, R. Picelli, H.A. Kim, Connecting microstructures for multiscale topology optimization with connectivity index constraints, J. Mech. Des. 140 (11) (2018) 111417.

[22] E. Sanders, A. Pereira, G. Paulino, Optimal and continuous multilattice embedding, Sci. Adv. 7 (16) (2021) eabf4838.

[23] N. Letov, Y. Fiona Zhao, Beam-based lattice topology transition with function representation, J. Mech. Des. 145 (1) (2023) 011704.

[24] J. Mueller, K.H. Matlack, K. Shea, C. Daraio, Energy absorption properties of periodic and stochastic 3d lattice materials, Adv. Theory Simul. 2 (10) (2019) 1900081.

[25] J. Wang, J. Huang, Functionally graded non-periodic cellular structure design and optimization, J. Comput. Inf. Sci. Eng. 22 (3) (2022) 031006.

[26] J.W. Cahn, On spinodal decomposition, Acta Metall. 9 (9) (1961) 795–801.

[27] A. Vidyasagar, S. Krödel, D.M. Kochmann, Microstructural patterns with tunable mechanical anisotropy obtained by simulating anisotropic spinodal decomposition, Proc. R. Soc. A: Math. Phys. Eng. Sci. 474 (2218) (2018) 20180535.

[28] M.-T. Hsieh, B. Endo, Y. Zhang, J. Bauer, L. Valdevit, The mechanical response of cellular materials with spinodal topologies, J. Mech. Phys. Solids 125 (2019) 401–419.

[29] F.V. Senhora, E.D. Sanders, G.H. Paulino, Optimally-tailored spinodal architected materials for multiscale design and manufacturing, Adv. Mater. 34 (26) (2022) 2109304.

[30] C.M. Portela, Fabrication, Mechanical Characterization, and Modeling of 3d Architected Materials Upon Static and Dynamic Loading (Ph.D. thesis), California Institute of Technology, 2019.

[31] G. De Schutter, K. Lesage, V. Mechtcherine, V.N. Nerella, G. Habert, I. Agusti-Juan, Vision of 3d printing with concrete—technical, economic and environmental potentials, Cem. Concr. Res. 112 (2018) 25–36.

[32] A. Chronicle, Cobod showcases 3d construction printing technology live at scale, 2022, https://amchronicle.com/news/cobod-3d-prints-construction-applications-live-in-front-of-record-breaking-audience-at-the-world-of-concrete-2022-in-las-vegas. (Accessed 23 January 2024).

[33] N. Hack, H. Kloft, Shotcrete 3d printing technology for the fabrication of slender fully reinforced freeform concrete elements with high surface quality: a real-scale demonstrator, in: Second RILEM International Conference on Concrete and Digital Fabrication: Digital Concrete 2020, Vol. 2, Springer, 2020, pp. 1128–1137.

[34] D. Weger, C. Gehlen, Particle-bed binding by selective paste intrusion—strength and durability of printed fine-grain concrete members, Materials 14 (3) (2021) 586.

[35] Voxeljet industrial 3d printing systems, 2017, https://www.voxeljet.com/. (Accessed 23 January 2024).

[36] D. Talke, K. Henke, D. Weger, Selective cement activation (sca)-new possibilities for additive manufacturing in construction, in: Proceedings of IASS Annual Symposia, International Association for Shell and Spatial Structures, IASS, 2019, pp. 1–8.

[37] H. Elsayed, F. Gobbin, M. Picicco, A. Italiano, P. Colombo, Additive manufacturing of inorganic components using a geopolymer and binder jetting, Addit. Manuf. 56 (2022) 102909.

[38] F.V. Senhora, O. Giraldo-Londono, I.F. Menezes, G.H. Paulino, Topology optimization with local stress constraints: a stress aggregation-free approach, Struct. Multidiscip. Optim. 62 (2020) 1639–1668.

[39] S. Kumar, S. Tan, L. Zheng, D.M. Kochmann, Inverse-designed spinodoid metamaterials, Npj Comput. Mater. 6 (1) (2020) 73.

[40] C. Talischi, G.H. Paulino, A. Pereira, I.F. Menezes, Polytop: a matlab implementation of a general topology optimization framework using unstructured polygonal finite element meshes, Struct. Multidiscip. Optim. 45 (2012) 329–357.

[41] M.P. Bendsøe, Optimal shape design as a material distribution problem, Struct. Optim. 1 (1989) 193–202.

[42] B. Hassani, E. Hinton, Homogenization and Structural Topology Optimization: Theory, Practice and Software, Springer Science & Business Media, 2012.

[43] E.D. Sanders, A. Pereira, M.A. Aguiló, G.H. Paulino, Polymat: an efficient matlab code for multi-material topology optimization, Struct. Multidiscip. Optim. 58 (2018) 2727–2759.

[44] B. Bourdin, Filters in topology optimization, Internat. J. Numer. Methods Engrg. 50 (9) (2001) 2143–2158.

[45] T. Zegard, G.H. Paulino, Bridging topology optimization and additive manufacturing, Struct. Multidiscip. Optim. 53 (2016) 175–192.

[46] J.K. Guest, J.H. Prévost, T. Belytschko, Achieving minimum length scale in topology optimization using nodal design variables and projection functions, Internat. J. Numer. Methods Engrg. 61 (2) (2004) 238–254.

[47] K.-J. Bathe, Finite Element Procedures, 2006, Klaus-Jurgen Bathe.

[48] J. Stegmann, E. Lund, Discrete material optimization of general composite shell structures, Internat. J. Numer. Methods Engrg. 62 (14) (2005) 2009–2027.

[49] J. Nocedal, S.J. Wright, Numerical Optimization, Springer, 1999.

[50] D.P. Bertsekas, Nonlinear programming, J. Oper. Res. Soc. 48 (3) (1997) 334.

[51] F. Gobbin, H. Elsayed, A. Italiano, J. Adrien, P. Colombo, E. Maire, Large scale additive manufacturing of artificial stone components using binder jetting and their x-ray microtomography investigations, Open Ceram. 7 (2021) 100162.

[52] K. Yu, Y. Guo, Y. Zhang, K. Soe, Magnesium oxychloride cement-based strain-hardening cementitious composite: Mechanical property and water resistance, Constr. Build. Mater. 261 (2020) 119970.

[53] M. Le Rouzic, T. Chaussadent, L. Stefan, M. Saillio, On the influence of mg/p ratio on the properties and durability of magnesium potassium phosphate cement pastes, Cem. Concr. Res. 96 (2017) 27–41.

[54] G. Dong, Y. Tang, Y.F. Zhao, A 149 line homogenization code for three-dimensional cellular materials written in matlab, J. Eng. Mater. Technol. 141 (1) (2019) 011005.

[55] A.G.M. Michell, Lviii. the limits of economy of material in frame-structures, Lond. Edinb. Dublin Philos. Mag. J. Sci. 8 (47) (1904) 589–597.

[56] O. Giraldo-Londoño, G.H. Paulino, A unified approach for topology optimization with local stress constraints considering various failure criteria: von mises, drucker–prager, tresca, mohr–coulomb, bresler–pister and willam–warnke, Proc. R. Soc. A 476 (2238) (2020) 20190861.

[57] P. Liu, L. Shi, Z. Kang, Multi-material structural topology optimization considering material interfacial stress constraints, Comput. Methods Appl. Mech. Engrg. 363 (2020) 112887.

[58] G.L. Goh, S. Lee, S.H. Cheng, D.J.S. Goh, P. Laya, B.S. Han, W.Y. Yeong, et al., Enhancing interlaminar adhesion in multi-material 3d printing: A study of conductive pla and tpu interfaces through fused filament fabrication, Mater. Sci. Addit. Manuf. 3 (1) (2024) 2672.

[59] C. Soyarslan, S. Bargmann, M. Pradas, J. Weissmüller, 3D stochastic bicontinuous microstructures: Generation, topology and elasticity, Acta Mater. 149 (2018) 326–340.

[60] V. Pini, J. Ruz, P.M. Kosaka, O. Malvar, M. Calleja, J. Tamayo, How two-dimensional bending can extraordinarily stiffen thin sheets, Sci. Rep. 6 (1) (2016) 29627.